

## ⓘ A Pan-Alpine Climatology of Lightning and Convective Initiation

AGOSTINO MANZATO,<sup>a,c</sup> STEFANO SERAFIN,<sup>b</sup> MARIO MARCELLO MIGLIETTA,<sup>c</sup> DANIEL KIRSHBAUM,<sup>d</sup>  
AND WOLFGANG SCHULZ<sup>e</sup>

<sup>a</sup> ARPA FVG–OSMER, Palmanova, Italy

<sup>b</sup> Department of Meteorology and Geophysics, University of Vienna, Vienna, Austria

<sup>c</sup> ISAC–CNR, Padua, Italy

<sup>d</sup> Department of Atmospheric and Oceanic Sciences, McGill University, Montreal, Quebec, Canada

<sup>e</sup> OVE Service GmbH–Department ALDIS, Vienna, Austria

(Manuscript received 16 June 2021, in final form 6 May 2022)

**ABSTRACT:** A new lightning-flash and convective initiation climatology is developed over the Alpine area, one of the hotspots for lightning activity in Europe. The climatology uses cloud-to-ground (CG) data from the European Cooperation for Lightning Detection (EUCLID) network, occurring from 2005 to 2019. The CG lightning data are gridded at a resolution of approximately 2 km and 10 min. A new and simple method of identifying convective initiation (CI) events applies a spatiotemporal mask to the CG data to determine CI timing and location. Although the method depends on a few empirical thresholds, sensitivity tests show the results to be robust. The maximum activity for both CG flashes and CI events is observed from mid-May to mid-September, with a peak at the end of July; the peak in the diurnal cycle occurs in the afternoon. CI is mainly concentrated over and around the Alps, particularly in northern and northeastern Italy. Since many thunderstorms follow the prevailing midlatitude westerly flow, a peak of CG flashes extends from the mountains into the plains and coastal areas of northeastern Italy and Slovenia. CG flashes and CI events over the sea/coast occur less frequently than in plains and mountains, have a weaker diurnal cycle, and have a seasonal maximum in autumn instead of summer.

**KEYWORDS:** Lightning; Climatology; Convective storms; Thunderstorms

### 1. Introduction

Lightning is a distinctive feature of thunderstorms. It forms due to electrical charge separation in deep, strong cumulus updrafts. For example, in the “noninductive mechanism” of lightning, relatively large rimed graupel/hail particles collide with small ice crystals, growing by vapor diffusion, in the presence of water like supercooled cloud droplets (e.g., Reynolds et al. 1957). In the warmer and liquid-rich lower portion of the cloud, the collisions tend to transfer positive charge to the graupel and negative charge to the crystals. The polarity of these transfers changes sign in the colder temperatures in the upper portions of the cloud (e.g., Takahashi 1978). Differences in terminal velocity between the larger, denser rimed targets and lighter ice crystals separate positive charge at lower levels from negative charge aloft (e.g., Saunders et al. 2006). The corresponding electric field can induce lightning flashes both within the cloud [intra-cloud or cloud-to-cloud (IC)] and from the cloud to the ground (CG).

High-amplitude electrical currents in CG strikes can damage life, property, and vital utility/communication networks. To mitigate these hazards and to better observe lightning, lightning-detection networks have been established in various countries, including but not limited to the United States (e.g., Biagi et al. 2007; Cummins and Murphy 2009), and

many European nations. Over the European continent, detection networks were developed independently in several countries (France, Germany–Switzerland, Italy, and Austria) during the 1980s. Data from these networks have served as the basis for analyses of the regional occurrence and intensity of thunderstorms (e.g., Finke and Hauf 1996; Steinacker et al. 2000). However, because each network differs in hardware and detection methods, extending such analyses to larger regions encompassing multiple networks is not straightforward (Poelman et al. 2016).

To produce a more seamless lightning detection network across Europe, the EUCLID (European Cooperation for Lightning Detection) consortium was established in 2001. Using about 180 sensors across Europe, EUCLID detects CG lightning strokes with nearly homogeneous and high quality, high location accuracy, and fine spatiotemporal resolution (Schulz et al. 2016; details provided shortly). EUCLID has already served as the basis for various analyses of thunderstorm and lightning occurrence over different portions of Europe (e.g., Piper and Kunz 2017; Mohr et al. 2019; Taszarek et al. 2019). With a CG data record of about 20 years, EUCLID is becoming increasingly suitable for long-term climatological analyses.

The present study focuses not only on the long-term CG climatology, but specifically also on the application of lightning data to identify thunderstorm initiation (or convection

ⓘ Denotes content that is immediately available upon publication as open access.

Corresponding author: A. Manzato, agostino.manzato@osmer.fvg.it



This article is licensed under a [Creative Commons Attribution 4.0 license](http://creativecommons.org/licenses/by/4.0/) (<http://creativecommons.org/licenses/by/4.0/>).

DOI: 10.1175/MWR-D-21-0149.1

© 2022 American Meteorological Society. For information regarding reuse of this content and general copyright information, consult the [AMS Copyright Policy](https://www.ametsoc.org/PUBSReUseLicenses/) ([www.ametsoc.org/PUBSReUseLicenses/](https://www.ametsoc.org/PUBSReUseLicenses/)).

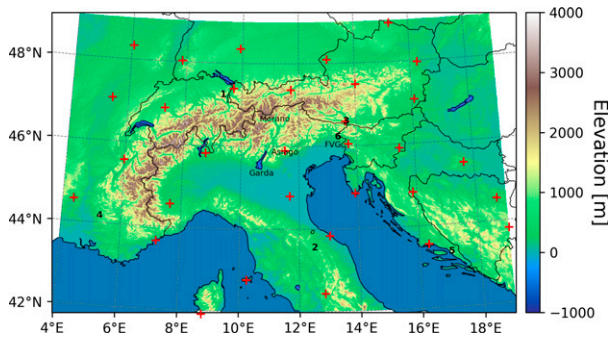


FIG. 1. The domain ( $42^{\circ}$ – $49^{\circ}$ N,  $4^{\circ}$ – $19^{\circ}$ E) where the EUCLID cloud-to-ground lightning flashes are studied. Red crosses show the EUCLID sensor locations, while the black numbers from 1 to 6 show Sântis Mount, Monte Nerone, Dobratsch Mount, Mont Ventoux, Sveti Jure Mount, and Gran Monte, respectively, which correspond to local spikes of the lightning climatology shown in Fig. 2.

initiation, hereafter abbreviated as CI) over the European Alps, a roughly southwest-to-northeast-oriented mountain chain, extending across several central European countries (France, Switzerland, Liechtenstein, Austria, Germany, Italy, Slovenia and Hungary, Fig. 1). Despite decades of intensive study on the subject, the understanding and prediction of CI remains an outstanding challenge of atmospheric science. This challenge stems from the inherent complexities of CI, including nonlinear and chaotic interactions between a wide range of processes on different scales (boundary-layer turbulence, cloud latent-heat release, mesoscale circulations, synoptic forcing, etc.). At a very basic level, two necessary conditions for CI are the existence of a region with nonzero convective available potential energy (CAPE) and the possibility that air parcels are lifted to their level of free convection (LFC). Jointly, these conditions favor CI in regions where warm and humid air masses are collocated with low-level updrafts (e.g., Markowski and Richardson 2010). The Alps have long been recognized as a regional hotspot of thunderstorm formation (e.g., van Delden 2001), due to the role of the terrain in favoring more unstable environments (e.g., weakening convective inhibition because the surface is closer to the LFC in mountain than it is in the plain) and the orographic lifting of potentially unstable air to its LFC. The mechanisms of Alpine lifting include both mechanical forcing, where impinging flow is forcibly lifted over or around the terrain, and thermal forcing, where elevated heating induces positive buoyancy and up-mountain flow (e.g., Kirshbaum et al. 2018).

Although climatologies of precipitation and thunderstorms have been variously performed in different parts of the Alps, using different datasets (e.g., weather reports in Costa et al. 2001; van Delden 2001, or lightning observations in Christian et al. 2003; Feudale and Manzato 2014; Anderson and Klugmann 2014; Enno et al. 2020; Taszarek et al. 2020), none have evaluated CI over the whole Alpine massif. As a result, the detailed spatiotemporal variations in Alpine CI remain inadequately understood. This shortcoming stems in part from inherent observational challenges and extreme spatial heterogeneity in flow properties over complex terrain.

While radar data are commonly used to detect CI by tracking thunderstorm cells in areas of continuous radar coverage (e.g., Rosenfeld 1987), these data are discontinuous over the Alps due to mountain beam blocking. When cells initiate within or traverse gaps in radar coverage during their life cycle, they cannot be tracked back to their origin. Other observations, like surface stations and radiosondes, are also scarce over high terrain due to practical challenges of instrumenting remote locations. Thus, while mountains represent natural laboratories for the study of CI, they also pose difficulties that greatly limit the ability to observe the CI process in detail. Given the above challenges, studies of Alpine CI have largely focused on subareas, where continuous radar cell tracking is possible, or they have merged radar with complementary datasets that are continuous over complex terrain. For example, Steinacker et al. (2000) and Bertram and Mayr (2004) used radar and/or EUCLID lightning data to track storms over Austria, and Weckwerth et al. (2011) used radar data to track storms over the lower Vosges (France) and Black Forest (Germany) Mountains just to the north of the main Alpine barrier. Nisi et al. (2016) also used radar storm tracking to investigate severe hailstorms over and around Switzerland.

The formidable difficulties in observing orographic CI over the entire Alpine massif can be partially overcome by using datasets that are continuous across mountain regions. Earth-observing satellites, for example, see cloud formation equally well over mountains and flat terrain. However, infrared satellite channels (e.g., Banta and Schaaf 1987) lack the resolution to capture the critical early phases of cumulus formation and growth, and visible channels are limited to the daytime hours (e.g., Mecikalski and Bedka 2006). Moreover, from satellite imagery alone, it may be difficult to unambiguously identify CI when incipient low-level clouds are obscured by upper-level clouds, which themselves may correspond to the anvil outflow of earlier thunderstorm cells. Lightning data also provides a viable means for tracking thunderstorms, provided sufficient spatial coverage and spatiotemporal resolution to track coherent storm cells over their life cycles and a good lightning detection efficiency.

In this study, we develop the first pan-Alpine climatology of thunderstorm occurrence and initiation, by exploiting the quality, continuity, and high spatiotemporal resolution of EUCLID cloud-to-ground (CG) lightning flash data over the Alps. Section 2 describes the EUCLID lightning flash data in more detail. Section 3 presents the spatial and temporal distributions of lightning occurrence, and section 4 presents the convective initiation definition and climatology, comparing it with the corresponding CG climatology. Section 5 summarizes the results.

## 2. Data and methods

### a. Data

The area of interest for this study encompasses the European Alps (Fig. 1). In particular, we consider the whole region between  $42^{\circ}$  and  $49^{\circ}$ N and between  $4^{\circ}$  and  $19^{\circ}$ E, for a total surface area of about 0.9 million  $\text{km}^2$ .

We analyze lightning observations collected by the European Cooperation for Lightning Detection (EUCLID) consortium

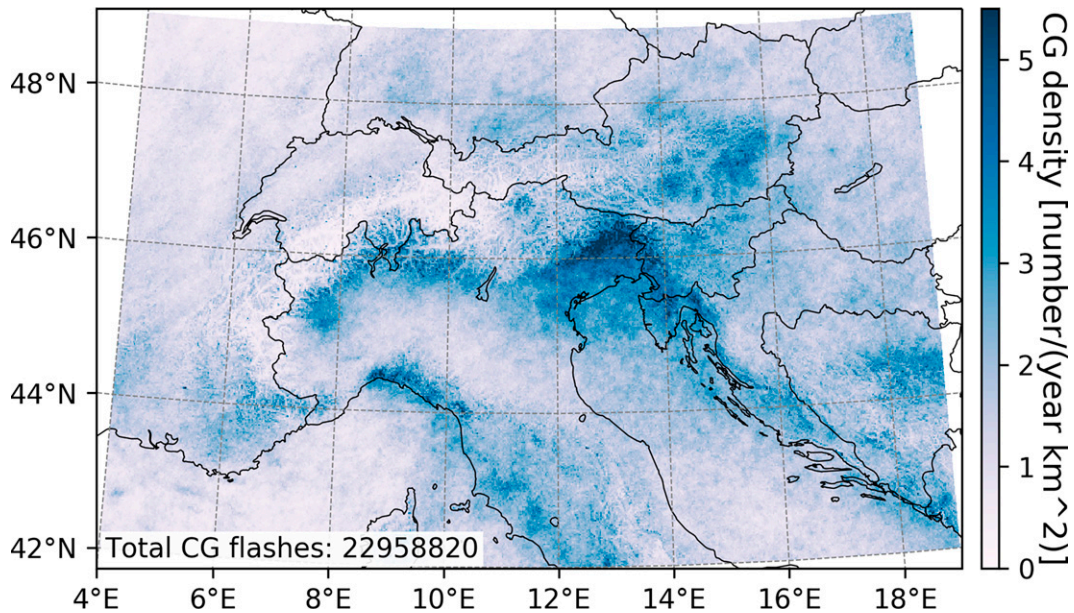


FIG. 2. Spatial distribution of CG  $\text{km}^{-2} \text{yr}^{-1}$  based on EUCLID data from 2005 to 2019.

and provided by the Austrian Lightning Detection and Information System (ALDIS, the Austrian partner of EUCLID). In 2020, the EUCLID network consisted of about 180 sensors distributed all over Europe. Sensor locations inside the studied domain are shown as red crosses in Fig. 1. The EUCLID cooperation merges sensor raw data from independent national networks and provides as output lightning data of high (Schulz et al. 2016) and nearly homogeneous quality, because the sensor type and the distance between the sensors are homogeneous in the region of investigation. Further, because of the used frequency bandwidth (1–350 kHz) for the EUCLID lightning location system (LLS), the orography has no impact on performance of the LLS.

During the years of operation, the network has been continuously improved by upgrading sensors to newer technology and by improving the location algorithm. The majority of sensors in the region use the latest available technology (Vaisala LS700x sensors), which is also able to detect CG and IC lightning data. These are the same sensors used in the U.S. National Lightning Detection Network (NLDN, Murphy et al. 2021). However, to avoid any influence of those improvements on the results, and to have a time series long enough for climatological purposes, we focus on the CG flash data only, which are available for 15 years with a homogeneous and high data quality. In contrast, IC lightning are homogeneously observed in this region only since 2015 and the EUCLID IC pulse-to-flash grouping algorithm has been active only since 2017. IC data available since 2017 form too short a database to study climatological behaviors; however, the appendix compares some results for 2017–19 using only CG flashes as well as using the total flashes (CG + IC).

The main performance parameters of a lightning location system (LLS) related to cloud-to-ground (CG) flashes are the location accuracy and detection efficiency. To provide

estimates of these performance parameters, there are ongoing comparisons of the EUCLID LLS data with ground truth data in Austria (Schulz et al. 2012; Diendorfer et al. 2014; Schwalt et al. 2020), Belgium (Poelman et al. 2013), and France (Pédeboy et al. 2014). For example, Schulz et al. (2016) showed that the performance estimates in Austria and France has a median location-accuracy of about 100 m (in both cases) and a CG flash-detection efficiency of about 97% and 90% for Austria and France, respectively.

Lightning data, available for the 15-yr period from 2005 to 2019, are aggregated every 10 min and every  $0.025^\circ$  in longitude (about 2.01 km) and  $0.020^\circ$  in latitude (about 2.13 km), so that each grid box covers an area of approximately  $4.3 \text{ km}^2$ . In roughly half (54%) of the approximately 0.79 million 10-min measurement intervals, there are no CG flashes in the studied domain. The total number of observed CG flashes is 22.96 million. The spatially and temporally averaged observed flash density is therefore approximately  $1.70 \text{ CG flashes km}^{-2} \text{ yr}^{-1}$  (cf. Fig. 2).

#### b. Methods

In general, data binned at 10-min intervals form the basis of our analysis. Data are not aggregated on longer intervals (e.g., hourly or yearly) unless explicitly specified. To facilitate comparison with other works, flash density is also reported as flashes  $\text{km}^{-2} \text{ h}^{-1}$  or flashes  $\text{km}^{-2} \text{ yr}^{-1}$  (multiplying by 6 or by 52560, respectively). Much of the subsequent analysis deals with comparing spatial distributions and temporal variability patterns of lightning flash density. Such comparisons need to account for the statistical properties of the flash density sample. In particular, the number of flashes per grid box in 10 min is a semi-bounded and highly skewed variable, with a markedly non-Gaussian distribution, a broad range of variability and a high degree of intermittency, i.e., long spells of zero

flashes interspersed with short periods of activity. Statistical dispersion around the mean value of flash density is therefore extremely high.

In an attempt to represent the degree of variability, where appropriate we display empirical quantiles of the sample. Because zero values comprise approximately half of the sample, we consider the 50th, 75th, 85th, and 90th (or 95th) percentiles. For instance, Fig. 9 in Zheng et al. (2016), Fig. 2 in Poelman et al. (2016), Fig. 4 in Piper and Kunz (2017), and Fig. 10 in Enno et al. (2020) all display mean diurnal cycles of lightning without reporting any information about the underlying variability.

When comparing spatial and temporal distributions of CG flashes and CI events (section 4), we consider differences between standardized variables. Original variables ( $X$ ) are transformed into standardized ones ( $Z$ ) according to

$$z_i = \frac{x_i - \bar{X}}{\sigma_X} \quad \forall x_i \in X, \quad z_i \in Z, \quad (1)$$

where the overbar denotes the mean of the sample and  $\sigma$  its standard deviation.

### 3. CG lightning climatology

#### a. Spatial distribution

A clear maximum of CG flash density is present in north-eastern Italy [Friuli Venezia Giulia (FVG)], while secondary maxima are found in northwestern Italy (pre-Alps and coastal areas), southeastern Austria, southeastern France, Dinaric Alps, and Slovenia (Fig. 2). The maximum of convective activity in northeastern Italy is consistent with the findings from Fig. 2 of Feudale and Manzato (2014), Fig. 5a of Punge et al. (2017, from satellite data) and Fig. 12 of Taszarek et al. (2020). In contrast, a relative minimum of flash density coincides with the main Alpine crest.<sup>1</sup> Thus, lightning is most frequent not over the highest terrain, but rather around the Alps, particularly along the southern slope, which is most exposed to warm, humid airflow from the south. The flash densities in Fig. 2 are consistent with comparable storm distributions over common regions of Europe (Anderson and Klugmann 2014; Kotroni and Lagouvardos 2016; Taszarek et al. 2019; Enno et al. 2020), northern Italy (Feudale and Manzato 2014), central Alps (Nisi et al. 2016), and Austria (Simon et al. 2017).

Pointwise maxima of climatological flash density (isolated peaks) coincide with transmitting towers and antenna buildings on a few specific mountain tops, at altitudes between 1525 m MSL (Monte Nerone, Italy) and 2502 m MSL (Sântis, Swiss), consistent with the findings from the U.S. NLDN by Kingfield et al. (2017). The locations of the most notable spikes are annotated in Fig. 1. In terms of domain-averaged density of instantaneous flash rates, the absolute maximum,

<sup>1</sup> The Alpine divide is clearly visible in Fig. 1 and largely coincides with the northern border of Italy, which is also marked in Fig. 2.

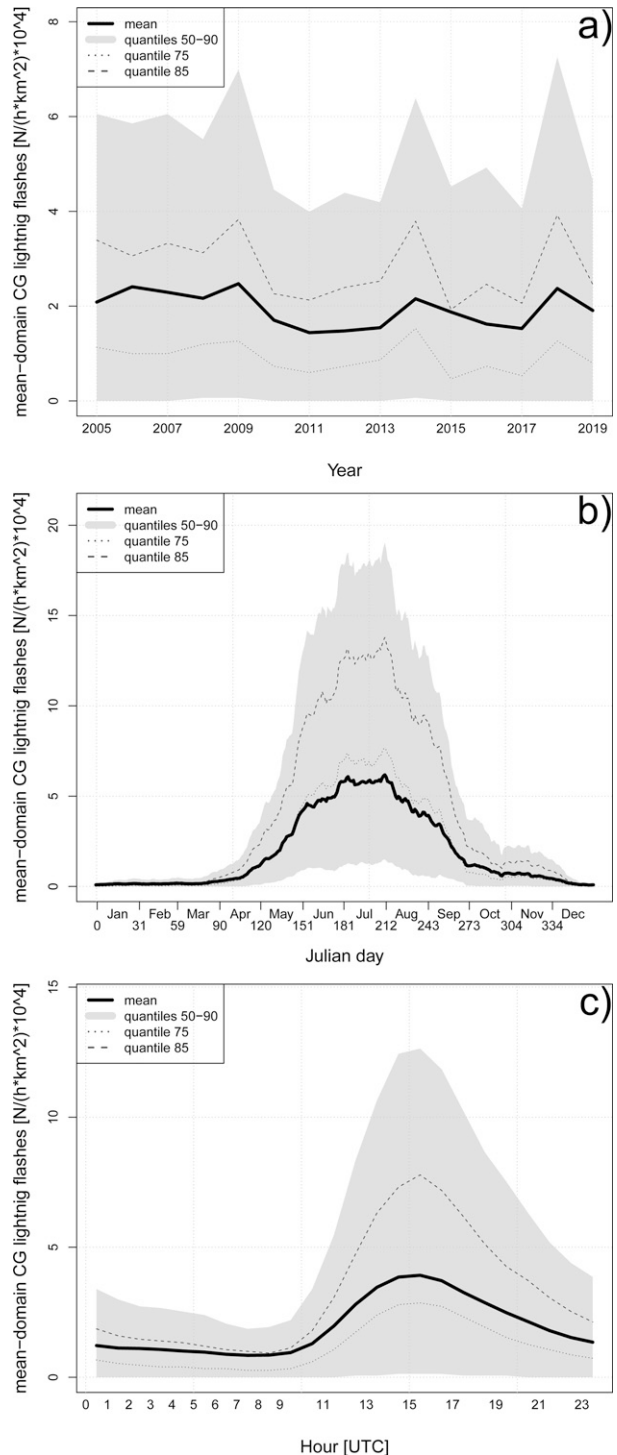


FIG. 3. Lightning flash density ( $\text{h}^{-1} \text{km}^{-2} \times 10^4$ ) vs (a) year, (b) day of the year (with a  $\pm 10$ -day moving average), and (c) time of day. The continuous line denotes the domain average; the shaded area shows the interval between 50th and 90th quantiles, while dotted and dashed lines show the 75th and 85th quantiles, respectively.

due to 2451 flashes observed between 1710 and 1720 UTC 26 May 2009, is equal to  $163 \times 10^{-4}$  flashes  $\text{km}^{-2} \text{h}^{-1}$ .

*b. Temporal distribution of the domain-averaged value*

Figure 3 shows the distribution of spatially averaged CG flash density versus year (also called interannual cycle, Fig. 3a), day-of-year (also called seasonal cycle, Fig. 3b) and hour of day (also called diurnal cycle, Fig. 3c). Due to the large statistical dispersion, the temporal variation of the mean values is small in comparison with quantile ranges. For example, in Fig. 3a, the year-to-year variability of the mean flash density is usually smaller than the variation between the 75th and 85th percentiles in each year.

No clear long-term trend can be identified in this relatively short time series. In fact, a linear fit between years and annual mean of CG density results in a low-correlation ( $R = 0.13$ ) negative slope, with low statistical significance ( $p$  value = 0.19).

The diurnal cycle of flash density (Fig. 3c) shows peak activity between 1500 and 1600 UTC (1600–1700 local solar time), which can be attributed to thermally driven convection. This finding is common to many lightning studies in different parts of the world, e.g., Zheng et al. (2016), Poelman et al. (2016), Piper and Kunz (2017), Nisi et al. (2020). Minimum flash densities occur typically in the early morning (0700–0900 UTC). Throughout the day, but in particular in the afternoon hours, variability around the mean diurnal cycle is very high.

Maximum lightning activity is observed between mid-May and mid-September, with a peak at the end of July (see  $\pm 10$ -day moving average in Fig. 3b). In particular, the spatial distributions of flash density during the most active months, from June to September, are shown in Fig. 4. While high flash density can be observed in the Alps in early and mid-summer (June–July, Figs. 4a,b) and in the Apennines in August (Fig. 4c), areas of maximum activity shift toward the coast or over the sea in September (Fig. 4d). This finding is in agreement with previous studies in the same region (Feudale et al. 2013, their Fig. 6; Feudale and Manzato 2014, their Fig. 6) and seems to be a common occurrence throughout the Mediterranean area and Europe (Kotroni and Lagouvardos 2016, their Fig. 2; Enno et al. 2020, their Fig. 8; Taszarek et al. 2019, their Fig. 4). The overall number of CG events in September is less than half of those in July, with the domain-averaged density similarly reduced from  $6 \times 10^{-4}$  to  $2 \times 10^{-4}$  flashes  $\text{km}^{-2} \text{h}^{-1}$ . The lightning activity in September is concentrated along the Tyrrhenian and the eastern Adriatic coast, with widespread activity in the extreme northern tip of the Adriatic Sea, and very weak activity along the western (Italian) Adriatic coasts.

To highlight the differences in temporal distributions between land and maritime areas, we follow the same approach used by Feudale and Manzato (2014). Hence, we divide the domain into three subareas: “sea and coast,” “plains,” and “mountains.” Figure 5 represents the three subareas, both at the maximum resolution of the CG flash density ( $0.025^\circ \times 0.020^\circ$ , Fig. 5a) and at the lower resolution at which CI events are defined in section 4a ( $0.125^\circ \times 0.100^\circ$  or  $5 \times 5$  original grid boxes; Fig. 5b).

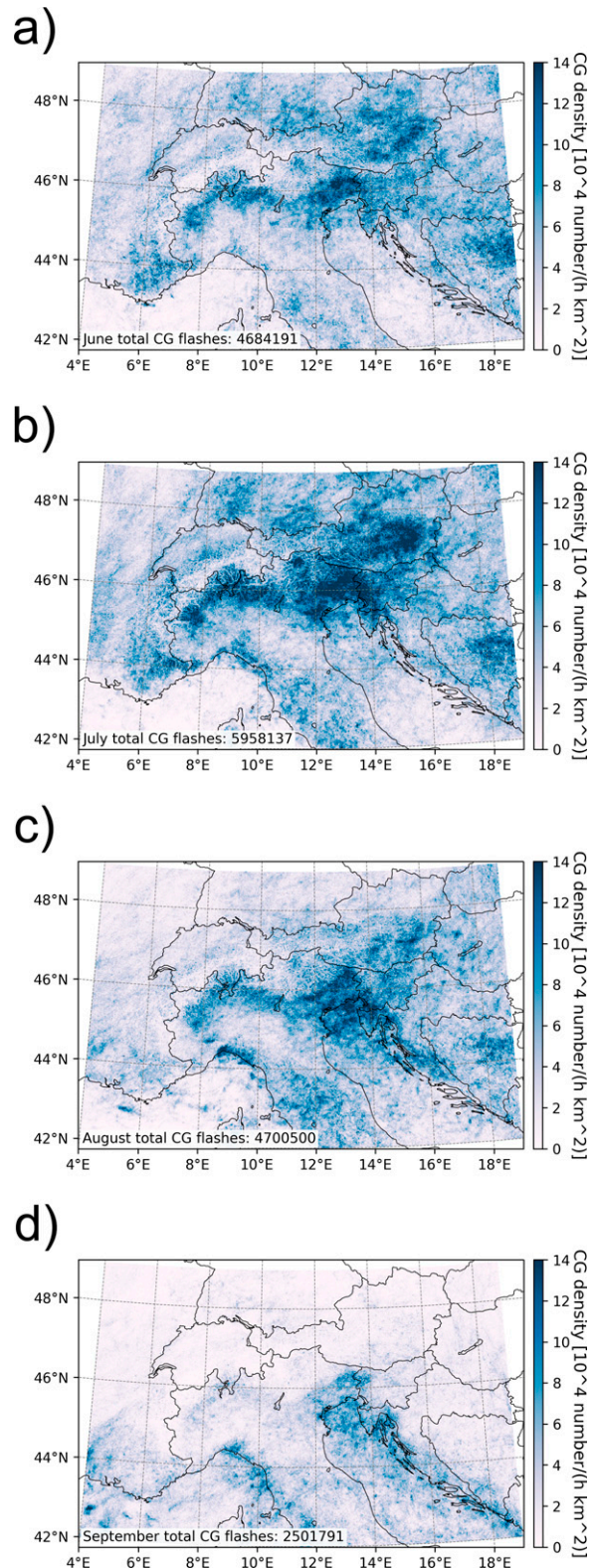


FIG. 4. The monthly climatology of EUCLID cloud-to-ground lightning flashes in the 2005–19 period ( $\text{h}^{-1} \text{km}^{-2} \times 10^4$ ) for (a) June, (b) July, (c) August, and (d) September.

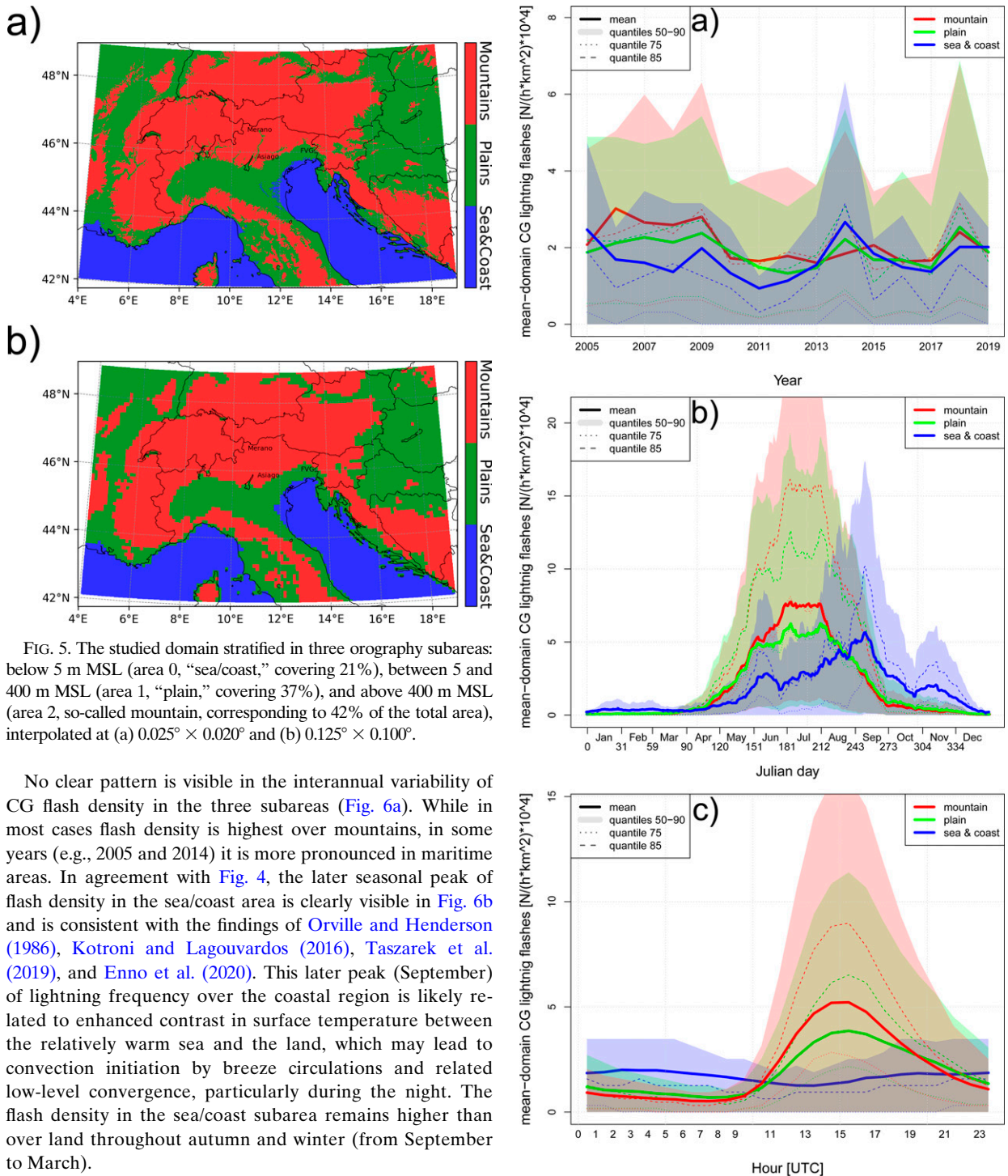


FIG. 5. The studied domain stratified in three orography subareas: below 5 m MSL (area 0, “sea/coast,” covering 21%), between 5 and 400 m MSL (area 1, “plain,” covering 37%), and above 400 m MSL (area 2, so-called mountain, corresponding to 42% of the total area), interpolated at (a)  $0.025^\circ \times 0.020^\circ$  and (b)  $0.125^\circ \times 0.100^\circ$ .

No clear pattern is visible in the interannual variability of CG flash density in the three subareas (Fig. 6a). While in most cases flash density is highest over mountains, in some years (e.g., 2005 and 2014) it is more pronounced in maritime areas. In agreement with Fig. 4, the later seasonal peak of flash density in the sea/coast area is clearly visible in Fig. 6b and is consistent with the findings of Orville and Henderson (1986), Kotromi and Lagouvardos (2016), Taszarek et al. (2019), and Enno et al. (2020). This later peak (September) of lightning frequency over the coastal region is likely related to enhanced contrast in surface temperature between the relatively warm sea and the land, which may lead to convection initiation by breeze circulations and related low-level convergence, particularly during the night. The flash density in the sea/coast subarea remains higher than over land throughout autumn and winter (from September to March).

The diurnal cycle (Fig. 6c) is most pronounced in mountainous areas, and less so over the plains. This feature is likely connected to thermally driven convergence of slope and valley breezes toward mountains, which locally enhances the likelihood of CI in comparison to the plains. In contrast, in coastal areas and over sea, the diurnal cycle is weaker and has an opposite phase, i.e., a diurnal minimum at midday and a relative nocturnal maximum between 0200 and 0400 UTC,

FIG. 6. Temporal distributions of the domain-averaged cloud-to-ground lightning flash number ( $\text{h}^{-1} \text{km}^{-2} \times 10^4$ ) as in Fig. 3, but stratified for the three orography-subareas shown in Fig. 5a: “sea/coast” (blue), “plain” (green), and “mountain” (red). Shaded area shows the interval between the 50th and 90th quantiles, while dotted and dashed lines show the 75th and 85th quantiles, respectively. Peaks are cut off to make the mean values more readable due to the very high skewness in the data distribution.

connected with land breezes propagating offshore. The opposite phases of the diurnal cycle over more continental (mountain and plain) versus more coastal/oceanic regions is consistent with numerous studies over different regions, including the pan-European climatology of [Enno et al. \(2020\)](#).

#### 4. Convective initiation climatology

##### *a. Identification of convection initiation events*

One can define convective initiation (CI) as the beginning of a storm track, possibly derived from radar or satellite remote sensing data, as explained in the introduction. A common radar-based approach for determining CI involves the tracking of coherent cells exceeding a reflectivity threshold (often in the 30–40-dBZ range) indicative of deep convection. The cell motion may be determined by overlap in cell location between consecutive scans or by matching extrapolated cell positions from previous scans with observed cell positions in subsequent scans. The location of cell initiation is then taken as the origin of the cell track (e.g., [Dixon and Wiener 1993](#); [Soderholm et al. 2014](#); [Nisi et al. 2018](#)). Multi-channel satellite data may also be used for storm tracking and CI determination (e.g., [Mecikalski and Bedka 2006](#); [Zimmer et al. 2008](#); [Kober and Tafferner 2009](#); [Walker et al. 2012](#)).

As previously mentioned, because radar data are discontinuous over the complex Alpine terrain, it cannot reliably be used for our CI detection. Satellite data are available, but the above-mentioned satellite cell-tracking methods generally require estimates of storm-motion vectors. Such estimates are uncertain because cell motion depends on cloud depth, cold pool propagation, and internal vortex dynamics (e.g., supercells), and may vary between different cells at a given time or between the same cell at two different times. These estimates are particularly uncertain over mountains, where cells may be anchored to certain terrain features and/or influenced by terrain-modified winds ([Soderholm et al. 2014](#)). Moreover, precise detection of CI location from satellite can suffer from issues like parallax error and imprecise estimation of cloud-top temperature ([Kaňák et al. 2020](#)).

Because lightning flashes are generally unique to deep convection, lightning may also be used alone, or in conjunction with satellite or radar data, to track thunderstorm cells and determine CI. However, existing methods for doing so also rely on uncertain storm-motion vectors ([Steinacker et al. 2000](#); [Bertram and Mayr 2004](#)). Given that we are only interested in CI and not in the entire storm track, we propose a somewhat simpler approach that avoids the uncertainties associated with estimating storm motion.

From lightning data alone, CI is defined herein as a cluster of  $5 \times 5$  grid points that has a certain number of CG lightning flashes (hereafter  $N$ ) in 10 min, when in the previous  $D$  minutes there were no other CI events in a surrounding radius  $R$ . In practice, the delay  $D$  and radius  $R$  define a spatiotemporal mask that should remove convection events already under way and leave only the newly initiated cells, which identify a convective initiation (CI) event. The CI events are studied on  $5 \times 5$  aggregated grid boxes (about  $10.1 \text{ km} \times 10.7 \text{ km}$ ,

covering about  $107 \text{ km}^2$ ), sufficiently large to fit the dimension of a typical storm cell in its initial phase (e.g., Fig. 5a in [Senf and Deneke 2017](#)). Smaller grid box sizes would increase the risk of splitting a single CI event over multiple grid boxes.

Given that different radar reflectivity thresholds are commonly used to track storms and identify CI events (e.g., [Dixon and Wiener 1993](#); [Soderholm et al. 2014](#); [Nisi et al. 2018](#)), some justification for our CG-based definition of CI may be useful. To begin, radar-based CI detection is very difficult over this pan-Alpine area, due to numerous gaps in high-resolution radar coverage, which prevents unambiguous and homogeneous identification of newly formed cells (see for instance Fig. 2 in [Kaltenböck and Steinheimer 2015](#)). Although, as one might expect, lightning tends to occur in areas of high radar reflectivity, radar- and lightning-based cell detections do not always agree. [Meyer et al. \(2013](#); their Fig. 4) compared the two detection methods over summer 2008 in southern Germany. While about 90% of total lightning-based cell detections corresponded to a radar-detected cell, about 60% of radar-detected cells were not connected with any lightning (IC or CG). The first finding confirms the ability of lightning networks to occasionally detect storms also in areas not accessible to radars. The latter suggests that some radar-detected “thunderstorms” actually produce no lightning (high radar reflectivity can be connected to shallow clouds not conducive to charge separation).

However, the definition of a “thunderstorm” (e.g., [American Meteorological Society 2021](#)) demands the presence of lightning, not any particular precipitation rate/size or radar reflectivity. Thus, a lightning-based detection method is not only more practical over the study region, but it is also more directly related to the presence of thunderstorms. The relationship between lightning occurrence and common metrics of storm intensity, such as updraft velocity and precipitation type/rate, remains uncertain. For example, [Deierling and Petersen \(2008\)](#) found that, beyond a certain vertical-velocity threshold ( $5\text{--}10 \text{ m s}^{-1}$ ), the total cloud flash rate depended primarily on updraft volume, not updraft strength. Moreover, large precipitation rates, comparable to those in midlatitude thunderstorms, often accompany warm-rain (and lightning-free) shallow convection in the tropics (e.g., [Smith et al. 2009](#)). Thus, while it is reasonable to suspect that more intense storms generally produce more lightning than weaker storms, we do not make inferences on storm intensity based only on the lightning data analyzed herein.

Note that new cells can be often triggered by pre-existing storms, a process that is sometimes called as “secondary convection” (e.g., [Ren et al. 2018](#)). In simulations of a few case studies in Germany, [Hirt et al. \(2020\)](#) discovered that up to half of all convective cells can originate from preexisting cells. In the present study, we will attempt to filter out such secondary initiations by appropriately tuning the parameters  $N$ ,  $R$ , and  $D$ .

To guide the design of the spatiotemporal mask, we refer to the thunderstorm characteristics derived from the radar climatologies in [Nisi et al. \(2018\)](#) and [Wapler \(2017\)](#), which tracked storms in Switzerland and Germany, respectively. In particular, from Figs. 15a(0) and 15b(0) of [Nisi et al. \(2018\)](#), the majority of storms (more than 75%) have a path shorter than 50 km and a duration shorter than 90 min, so we assign these

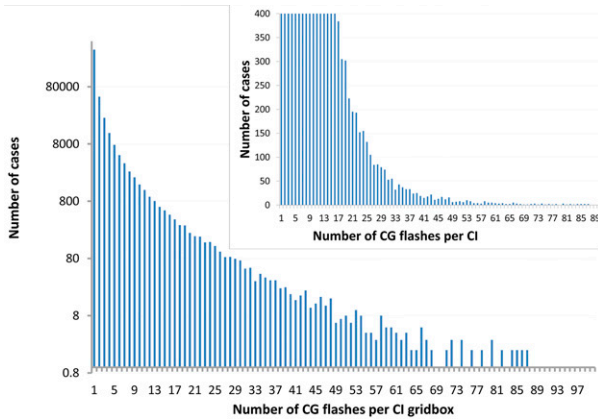


FIG. 7. Number of CG cases vs lightning flash density per CI grid box for all the candidate convective initiation events with less than 100 CG in 10 min. Counts are shown with a logarithmic scale, while in the top-right inset a zoom of the 0–400 range is shown with a linear scale.

values to  $R$  and  $D$  as a first guess. Moreover, also the sensitivity to different ranges of the number of CG flashes inside the CI grid box, indicated by  $N$ , will be discussed in the next section.

*b. Spatial distribution of CI*

The distribution of the number of flashes (in 10 min) inside each  $5 \times 5$  grid boxes considered as a candidate CI event, is shown in Fig. 7. This number might be expected to monotonically decrease, but the close-up view in the top-right quadrant of Fig. 7 shows that the monotonicity is lost beyond 20 CG flashes and, particularly after 30 CG flashes, there are some

fluctuations. Despite the fact that data tends to become noisier when the sample size decreases, in the range 20–30 CG flashes per CI candidate event there are between 223 and 74 cases per bin, so that the mean estimate is expected to be statistically robust. We interpret these fluctuations as the natural monotonic decreasing distribution summed up with another one, that we identify as the distribution of “mature-phase” storms. In an effort to avoid the more mature cells, the CI candidate events having a number of CG flashes,  $N$ , larger than 20 or 30 (both thresholds will be tested for sensitivity) will not be considered as “new” CI events.

The mature cells may not have been detected in their earlier stage, because they were inside the spatiotemporal mask of other storms (close in space or time). Alternatively, they might have already been counted as a CI event, but were able to break through the spatiotemporal mask, because they lasted more than 90 min or traveled for more than 50 km. In the latter case, the filter on the maximum  $N$  is used to avoid a double count of the large storms able to exceed the spatiotemporal criteria, because in their mature stage they likely produce more than 30 CG flashes in 10 min in  $5 \times 5$  grid boxes. Last, since cases having only one CG flash in 10 min do not always represent a robust signal of thunderstorm occurrence and sometimes could be contaminated by significantly mislocated strokes (that may pop up in the data before 2015) also a lower limit will be tested, selecting only cases having  $N \geq 2$  instead of  $N \geq 1$ .

Figure 8 shows the CI spatial distribution (as number of CI events  $\text{km}^{-2} \text{h}^{-1}$ ), defining as CI events all the  $0.125^\circ \times 0100^\circ$  (about  $10.1 \text{ km} \times 10.7 \text{ km}$ ) grid boxes satisfying  $2 \leq N \leq 30$ , while in the previous 90 min (from the beginning of the considered 10-min period) there were no other CI events in the neighborhood radius of 50 km. Comparing this CI density

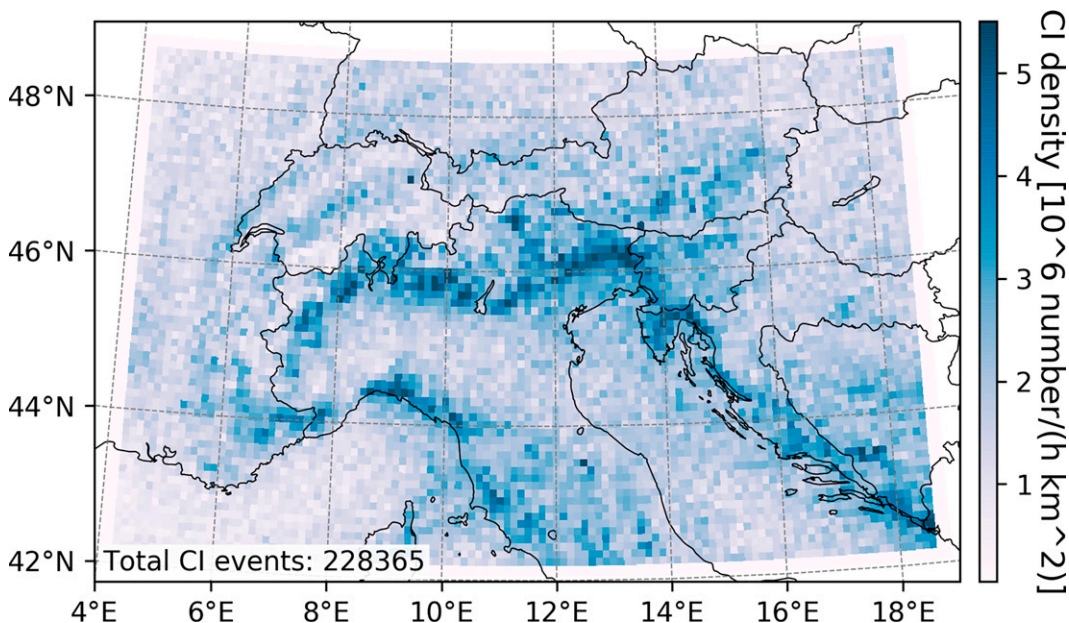


FIG. 8. The density of convective initiation events, derived from EUCLID cloud-to-ground lightning flashes re-gridded at  $10.1 \text{ km} \times 10.7 \text{ km}$ , as total occurrences per 10 min and  $\text{km}^2 \times 10^6$ , during the 2005–19 period. The parameters chosen to define CI are  $2 \leq N \leq 30$ ,  $D = 90 \text{ min}$ , and  $R = 50 \text{ km}$ .

with the CG density of Fig. 2 one can note many similarities, with the maximum located on the southern side of the Alps. However, there are also some differences: for example, CI has a local maximum on the pre-Alps located at the western side of the Garda Lake, which is comparable with the CI maximum located on NE Italy, while it was not present in the CG spatial distribution. More details on these subtle differences are provided below.

With the chosen parameters, around 228 000 CI events are found in the whole database. Of all the 10-min periods studied, only 0.14 million out of them (17.9%) contain at least one CI event inside the studied domain; thus, CI events occur for less than one fifth of all periods, on average. Looking only at the subset of the 10-min periods having at least one CI event in the domain, the average number of CI is 1.6 events  $(10 \text{ min})^{-1}$ . Summing together all the CG flashes contained inside these CI grid boxes, one obtains around 851 000 flashes, which are only 3.7% of the total CG flashes.

Comparing the domain-averaged value of CG flashes  $(1.9 \times 10^{-4} \text{ km}^{-2} \text{ h}^{-1})$  with that of all CI events  $(1.9 \times 10^{-6} \text{ km}^{-2} \text{ h}^{-1})$  there are 100.5 CG flashes per CI event. This number can be interpreted as an averaged number of CG flashes in the domain associated to each CI event. Since storms initiated by “secondary convection” (inside the spatiotemporal mask) are not counted as CI events, but they are counted in the total number of CG flashes, the mean number of CG flashes associated to each “storm” is actually lower than 100.5. Considering instead only the grid boxes identified as CI events, each CI event has on average 3.7 CG flashes (in 10 min and  $10.1 \text{ km} \times 10.7 \text{ km}$ ).

To study the sensitivity of the CI definition to the parameters chosen, Fig. 9 shows the corresponding climatologies that are obtained by replacing  $2 \geq N \geq 30$  with  $1 \geq N \geq 20$  (Figs. 9a,b), or replacing the spatiotemporal mask  $D = 90 \text{ min}$  and  $R = 50 \text{ km}$  with a smaller mask, in which  $D = 60 \text{ min}$  and  $R = 30 \text{ km}$  (Figs. 9b,c). While the total number of events changes when these parameters are varied, the basic spatial patterns, including the locations of relative minima and maxima, remain the same. Basically, removing the  $N = 1$  cases and using the more restrictive spatiotemporal mask (Fig. 8) improves the contrast of the image and increases the probability that the CI events were really new cells, even if some marginal CI events may have been filtered out during the process.

Another way to test the differences shown in the sensitivity analysis and, at the same time, to investigate the differences between CI and CG spatial distributions, can be obtained computing the anomaly fields of the different CI results with respect to a given reference, which is the CG spatial distribution of Fig. 2. When two spatial fields are compared for similarities/differences (e.g., to see if areas of local minima and maxima are collocated), it is common to analyze the differences of their anomalies. Since CG flashes and CI events are very different fields (with both different mean and variance), here the difference is made between the anomalies divided by the respective variance, i.e., between the fields standardized using Eq. (1). In practice, this difference highlights the areas where local minima or maxima of the two fields correspond to each other. We refer to this difference between the standardized CI and CG densities as CG flash “efficiency” per CI event. Where it is greater than zero

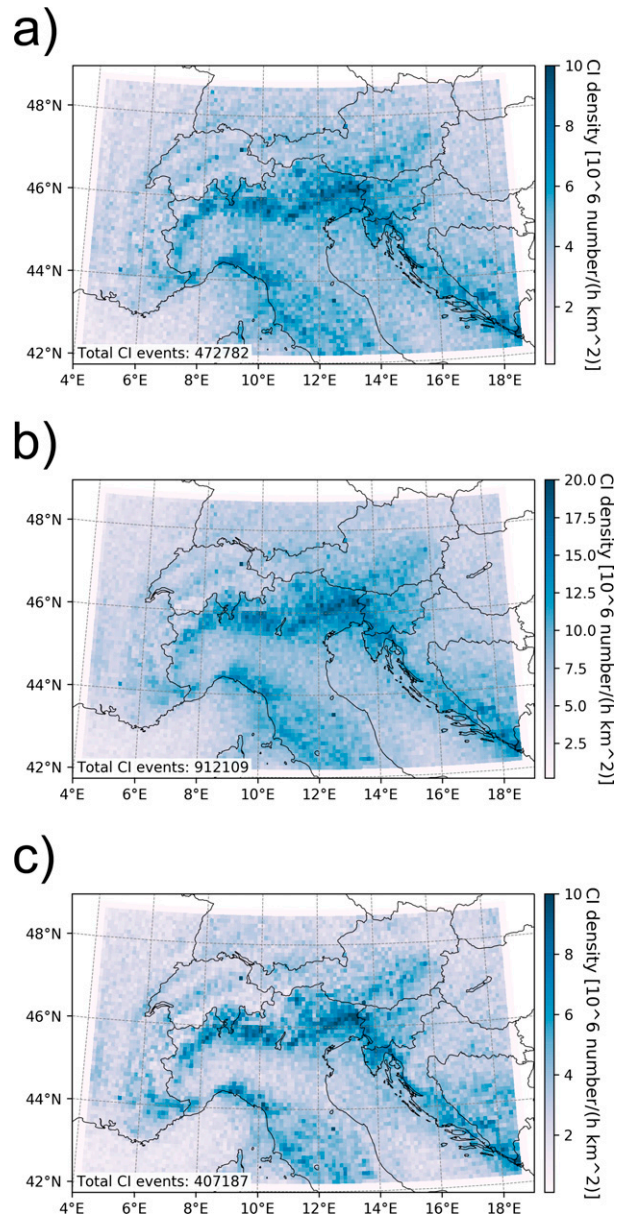


FIG. 9. Sensitivity of the convective initiation spatial distribution (as shown in Fig. 8) to different values of the parameters used to define a CI event. A CI event is defined if there are (a),(b)  $1 \leq N \leq 20$  or (c)  $2 \leq N \leq 30$  CG flashes in 10 min in the  $10.1 \text{ km} \times 10.7 \text{ km}$  grid box if there were no other CI occurrences in the (a)  $D = 90 \text{ min}$  or (b),(c)  $D = 60 \text{ min}$  before in a radius of (a)  $R = 50 \text{ km}$  or (b),(c)  $R = 30 \text{ km}$  around it, respectively. Note that scales (right side) and total number of CI event identified (bottom-left corner) are different for each panel.

(yellow areas in Fig. 10), CG flashes occur more frequently than their average ratio (i.e., 100.5 CG per CI).

The standardized version of the four CI spatial distributions of Figs. 8 and 9 have been subtracted from the same standardized spatial distribution of CG flashes (Fig. 2), permitting a comparison of the excess/lack of total CG associated with any

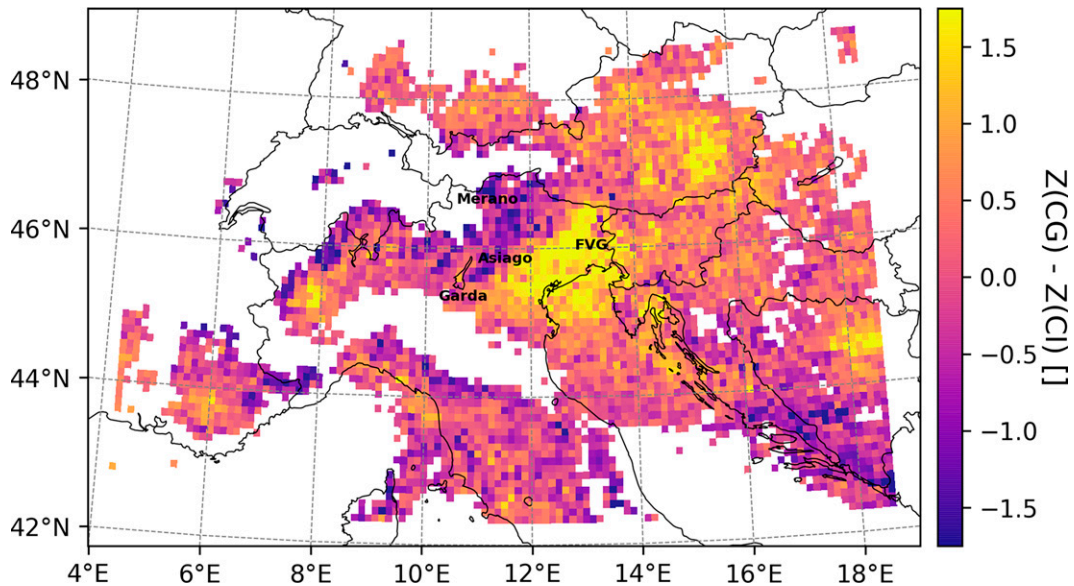


FIG. 10. Standardized total cloud-to-ground spatial distribution with respect to the standardized convective initiation spatial distribution, both re-gridded at  $10.1 \text{ km} \times 10.7 \text{ km}$  every 10 min for the same parameters used to define a CI event in Fig. 8. Grid boxes having less than 2500 total CG flashes in the 15 studied years are not displayed.

given density of CI events. Figure 10 shows this comparison for the parameters defining the CI spatiotemporal mask and  $N$  filter used in this work. Note that only grid boxes having more than 2500 CG flashes (subjective threshold) during the whole studied period have been displayed, in order to show only areas with a meaningful density of CG flashes. Based on Fig. 10 and on the corresponding three figures (not shown) computed with the set of CI parameters used in Fig. 9, we found that all of them have the same general pattern.

It is reasonable to assume that areas affected by a greater number of CG flashes, relative to the underlying CI event density, are likely affected by more intense/mature storms, while areas affected by smaller CG flashes relative to CI events are likely affected by weaker or initial-stage storms, that move out of the area sooner. While the maximum CI density is located in NE Italy (as it is for the CG maximum), the density of CG on its eastern side is relatively higher than expected from the CI spatial distribution and, on its western side, the density of CG lightning flashes is smaller than expected. Focusing on Northern Italy in particular, there are low values of standardized CG flashes minus CI events above the pre-Alps, around the Garda Lake and the Asiago Plateau extending northward, toward the city of Merano. Hence, that area seems to be a hotspot of CI events relative to the total CG flashes. Given that the dominant large-scale circulation in the midlatitude Alpine region is zonal (westerlies), it seems reasonable, also by comparing Fig. 2 with Fig. 8, that storms initiated along the pre-Alps reach maturity as they travel eastward, producing an excess of CG flashes over the plains and coastal areas of the very northeastern part of Italy and in western Slovenia (corresponding to the well-known CG lightning hotspot described in Feudale and Manzato 2014).

The possibility of cells initiated at a particular time strengthening over several hours may seem inconsistent with the previous assumptions underlying our spatiotemporal mask for CI events. However, this is not the case because, while individual cells usually do not live longer than 90 min or propagate farther than 50 km, large mesoscale systems (like multicells, squall lines, or MCS) originated by them can survive much longer (Hagen et al. 2000; Wapler 2017; Nisi et al. 2018) and travel farther than any individual cell. However, if they produce more than  $N = 30$  CG flashes in 10 min when they break the spatiotemporal mask, they are not counted as new CI events. These findings are also compatible with an evolution of storms initiated over the pre-Alps that propagate toward the plain (that is usually loaded with high values of equivalent potential temperature advected from the Adriatic Sea), possibly driven by cold-pool propagation effects (Miglietta et al. 2016; Pucillo et al. 2020). For this reason, NE Italy has not only the absolute maximum of CI events, but also receives lightning from mature storms that were initiated to the west and, under the prevailing westerly flow aloft, propagated into the region. These two effects together can explain the prominent maximum of CG flashes observed in the FVG region.

Something similar, although not as pronounced, happens on the eastern side of the studied domain (over the country of Bosnia and Herzegovina), with a relative minima of CG (as expected from the CI spatial distribution) located on the Dinaric Alps and an excess of CG total flashes on its NE side (Fig. 10). In both cases, the density of CI events is higher above complex orography, while the density of CG flashes has a relative maximum *leeward* (east) of the mountains.

As mentioned in section 2, our exclusive focus on CG in this analysis omits intra-cloud (IC) flashes, which typically are

much more frequent than CG flashes. Thus, it likely underestimates, and may also introduce some bias, into the CI climatology. Therefore, although EUCLID IC data are only available (and reliable) back to 2017, we perform an analogous spatial CI distribution using the combination of CG + IC in the appendix. This analysis reveals a high degree of similarity between the two distributions, suggesting that our focus on CG alone data does not appear to bias the CI climatology.

*c. Temporal distributions*

The temporal distributions of CI events are now analyzed and compared with those of the CG flashes, to evaluate the relation between storm initiation and total frequency of observed flashes on a yearly, monthly, daily basis. Henceforth, only the parameters of Fig. 8 will be used ( $D = 90$  min,  $R = 50$  km and  $2 \geq N \geq 30$ ). Figure 11 shows a similar temporal distribution as in Fig. 3, but for the CI events.<sup>2</sup> While the diurnal and seasonal cycles are similar to those of the CG flashes, the interannual trend is much flatter, with basically *no changes* in the quantiles (cf. in particular Fig. 3a with Fig. 11a). Thus, this statistic seems to be quite constant across the full dataset. The mean value is about  $1.9 \times 10^{-6}$  CI km<sup>-2</sup> h<sup>-1</sup>, which means about  $0.46 \times 10^{-4}$  CI km<sup>-2</sup> day<sup>-1</sup>. Considering that the full domain is  $0.9 \times 10^6$  km<sup>2</sup>, this means about 40 CI events per day in the whole domain. The  $\pm 10$ -day moving average of the mean CI value also has a rather flat peak from June to early August (Fig. 11b). In June–July one can expect up to  $5 \times 10^{-6}$  CI km<sup>-2</sup> h<sup>-1</sup>, which means about  $10^{-4}$  CI km<sup>-2</sup> day<sup>-1</sup> or 90 CI events per day in the whole domain. Figure 11c shows that the diurnal cycle of CI peaks 1 h before the maximum CG diurnal peak (1400–1500 UTC instead of 1500–1600 UTC; cf. with Fig. 3c), hence it is likely that the maximum CG activity occurs 1 h after the corresponding CI, on average.

Figure 12 shows the same three temporal distributions of Fig. 11, but stratified for the three subareas shown in Fig. 5b. In general, the mean value of CI events over the sea/coast subarea is much smaller than that over the mountain. When there are few classes (e.g., Figs. 12a,c) the number of 10-min periods with CI in the sea/coast subarea is so low, with respect to the total number of 10-min periods, that even the 95% quantile is almost always zero. The percentage of CI events over the mountain to the total CI events is 49.9%, while the percentage of CG flashes observed over the mountain is 45.6%, suggesting again that some of the storms initiated over mountains can then produce an excess of lightning flashes on the plain and coast where they move (e.g., Bertram and Mayr 2004). From October to February, the CI probability is much higher over the sea/coast subarea (66%) than it is over the plain (19%) and mountain (15%) zones (Fig. 12b), while from March to September the opposite is true (27%, 33%, and 40% for sea/coast, plain, and mountain, respectively). The high heat capacity of the Mediterranean Sea, and its

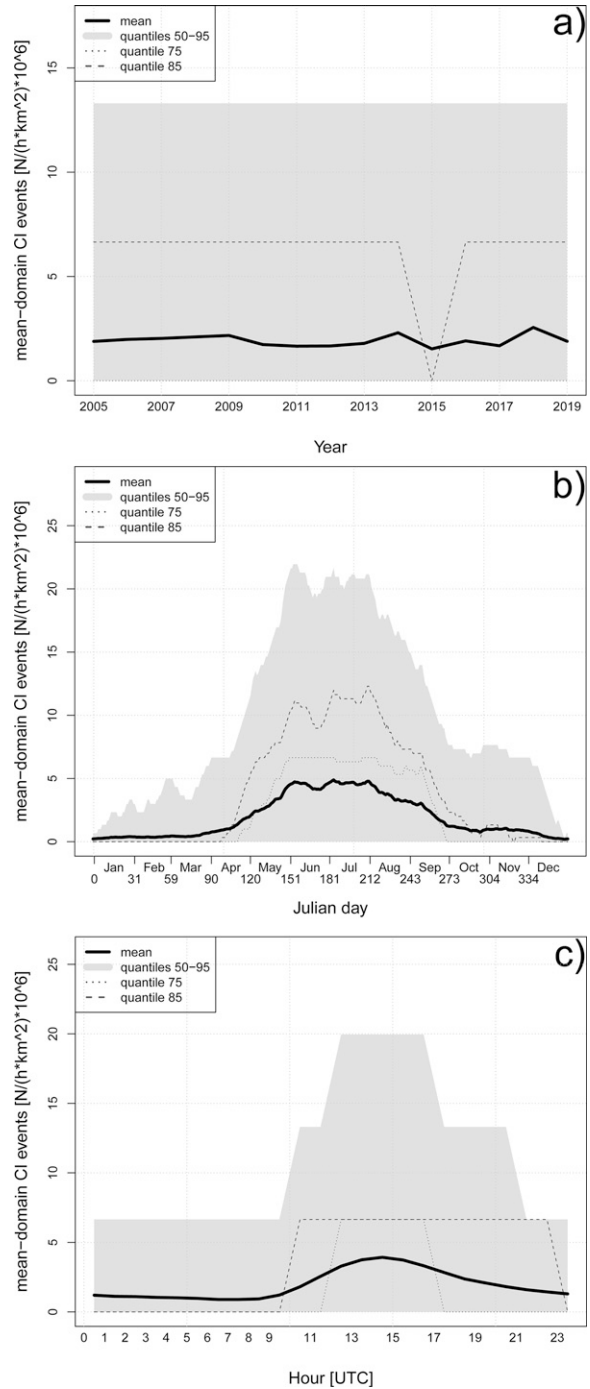


FIG. 11. Climatology of the domain-averaged convective initiation events ( $\text{h}^{-1} \text{km}^{-2} \times 10^6$ ) (a) for each of the 15 studied years, (b) for the day-of-year after applying a  $\pm 10$ -day moving average, and (c) for each hour of the day. The shaded area shows the interval between the 50th and 95th quantiles, while dotted and dashed lines show the 75th and 85th quantiles, respectively. Peaks are cut off to make the mean values more readable due to the very high skewness in the data distribution.

<sup>2</sup>The only difference with Fig. 3 is that here we show the 95th quantile instead of the 90th, because the number of zero cases is much higher for the CI events than it was for the CG flash number.

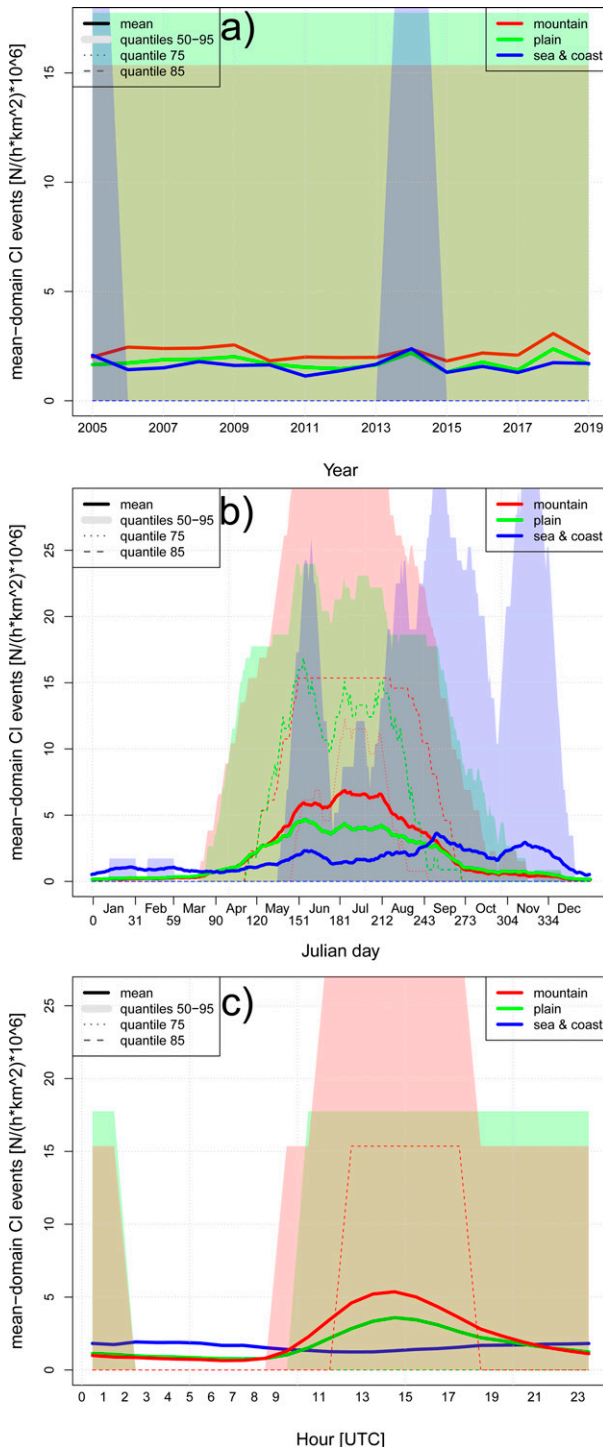


FIG. 12. Climatologies of the convective initiation events ( $\text{h}^{-1} \text{km}^{-2} \times 10^6$ ) as in Fig. 11, but stratified for the three orography-subareas shown in Fig. 5a: “sea/coast” (blue), “plain” (green), and “mountain” (red). The shaded area shows the interval between the 50th and 95th quantiles, while dotted and dashed lines show the 75th and 85th quantiles, respectively.

correspondingly warmer sea surface temperatures, is a major source of instability during the winter season (e.g., Galanaki et al. 2018). Very little diurnal variation of CI is found in the sea/coast subarea, while the diurnal cycle is much more pronounced in the mountain subarea (Fig. 12c).

#### d. Comparison of standardized CG and CI temporal distributions

A more quantitative comparison between the temporal distribution of CG flashes and CI events can be obtained by considering the difference of the standardized variables, following an approach similar to that considered in Fig. 10 for the spatial distribution. Figure 13 shows the difference between the standardized domain-mean value of CG flashes and the standardized domain-mean value of CI events for their year, day of the year, and hour of the day distributions. That is, the mean values in the three temporal distributions of Figs. 3 and 11 have been standardized subtracting the absolute mean and dividing by the standard deviation, both computed along each time period. As before, the standardization of (1) makes two very different fields more comparable. Given the different nature (and intrinsic variability) of these two fields, no attempt to draw confidence intervals has been done in this case.

Figure 13a shows a relatively large difference and large annual variability between CG and CI distributions, with a peculiar peak in 2015 (likely due to difficulties with sensor calibration and/or location errors after instrumentation upgrade to LS7002), and much smaller differences in the monthly and diurnal cycles (Figs. 13b,c).

In May the mean value of CG per CI reaches an absolute minimum, indicative of a lower efficiency in the CG production per CI event. This likely stems from the smaller instability, which prevents the storms from evolving into large structures producing many CG flashes, while potential lifted instability is much larger in July–August [cf. most unstable lifted index cycle in Fig. 5a of Manzato (2007)]. The same happens at about 1100 UTC of the diurnal cycle, while the CG production per CI is above normal at 1800 UTC. Consistently with previously mentioned arguments on the diurnal cycle, that could be due to the evolution of some storms, initiated at around midday (the CI maximum is centered between 1300 and 1600 UTC), into larger and more organized systems (e.g., MCS), reaching their most intense phase about 3–4 h later.

Figure 14 shows the same standardized temporal distributions as in Fig. 13, but stratified by subarea. The behavior of the seasonal and diurnal cycles over plain and mountain subareas are remarkably similar, while the CG-production efficiency exhibits different behaviors in the sea/coast subarea. For example, in the sea/coast the CG efficiency is much higher for CI events occurring in August than for those occurring in November, differently from the plain and mountain subareas. In fact, over the sea/coast there are more CI events in November than in August (Fig. 12b), but there are more CG flashes in August than in November (Fig. 6b), probably because of the more moist-unstable summertime environments. This behavior

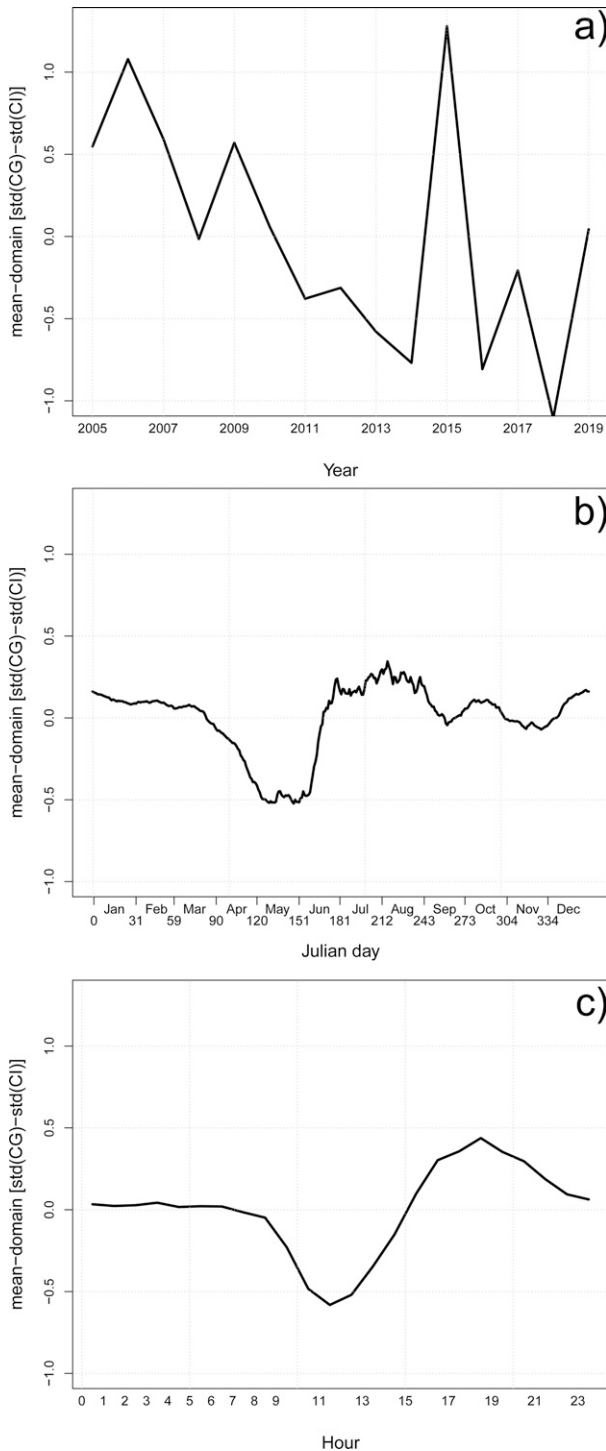


FIG. 13. The difference between the standardized domain-averaged CG lightning flashes and the standardized domain-averaged convective initiation climatologies (a) for each of the 15 studied years, (b) for the year day (difference between the two  $\pm 10$ -day moving average of the two standardized time series); and (c) for each hour of the day.

could also stem from differences in sea-surface temperature between August and November or from the differences between maritime and continental clouds, which are characterized by different electrification processes (Takahashi 1984; Orville and Henderson 1986). In particular, considering that non-inductive charging is the main driver (cf. chapter 3 in Rakov and Uman 2003), higher ice production (specifically graupel and small ice) will tend to cause higher flash rates.

*e. Temporal distributions of the number of CG per CI*

Time series of 10-min CG data are often correlated over short times, because a storm, present at a given time, is likely to also be present in the following 10-min periods, and often there are long sequences of the same value, i.e., zero density. For this reason, it could be interesting to study a subset of mostly uncorrelated CG data. By default, every CI event has a number  $N$  of CG flashes varying from 2 to 30. One can study the distribution of the special subset of these “first” CG flashes, being produced in the early stage of storms, i.e., those collected inside the about 228 000 CI events and representing only a minority (3.7%) of all the total CG data (Fig. 15). The CI grid boxes are well separated in time and space from each other (because of the spatio-temporal mask used to identify the CI grid boxes), and thus this dataset is made of relatively independent (uncorrelated) flashes.

Figure 15a shows that there is a weak relation (e.g., the maximum in 2015) between the interannual number of CG flashes in the CI events and the corresponding behavior for the total number of CG (Fig. 3a) or for the CI events (Fig. 12a). Figure 15b shows the seasonal cycle, with an average number of CG flashes in the CI grid boxes exceeding 3.5 between the end of May and mid-October, with a peak somewhat broader than that for the total number of CG flashes or for the number of CI events (Figs. 3b and 12b, respectively).

Last, Fig. 15c shows that the mean number of “first” CG flashes has small diurnal variations. Near sunrise and even more toward sunset, on average, the CI events are associated with a larger number of CG flashes than during midday. For example, between 1500 and 1800 UTC the 85th quantile shows a larger ability to produce many CG flashes in the very early stage of cell life, while between 0900 and 1100 UTC (between 1000 and 1200 local solar time) the mean value has an absolute minimum, suggesting that the corresponding storms exhibit a weaker lightning activity in their early stage. A possible explanation is that at midday radiative forcing is maximum, strong nocturnal inversions are lacking and consequently convective inhibition reduced (Kirshbaum et al. 2018), causing a peak in the frequency of thermally forced storms. If one supposes that CI from thermally forced storms start in a weaker way than CI triggered in other ways (e.g., by sudden synoptic large-scale forcing) that would explain the lower number CG inside the CI events at midday. Similar reasoning can explain the minimum in late spring-early summer shown in Fig. 13c (in May or June weaker thermally forced storms form compared to July–August, when the instability is greater and the intensity stronger).

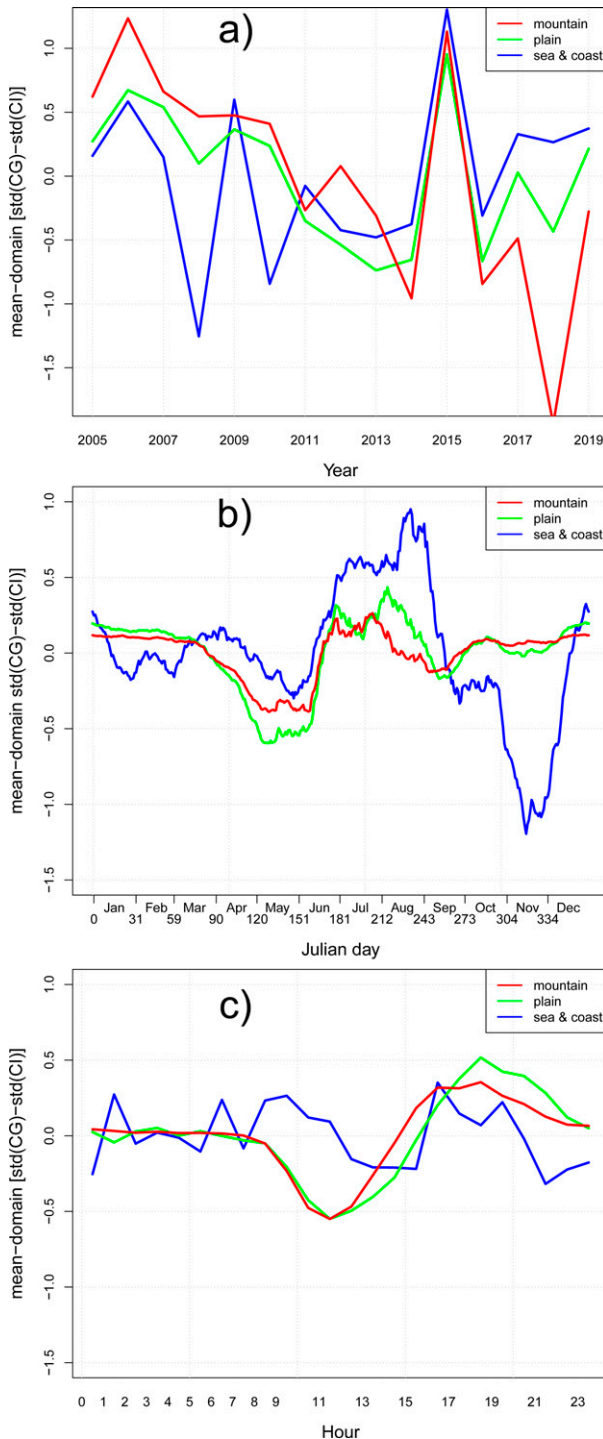


FIG. 14. The climatology of the difference between the standardized CG flashes and the standardized convective initiation events as in Fig. 13, but stratified for the three orography subareas shown in Fig. 5a: “sea/coast” (blue), “plain” (green) and “mountain” (red).

## 5. Summary

In this work, the first climatology of convective initiations (CI), defined as the first evidence of new convective cells, is

developed over a pan-Alpine domain, using high spatial and temporal resolution cloud-to-ground (CG) lightning data. Commonly, a CI event is identified in correspondence with the first radar echo or the first satellite brightness temperature above a critical threshold (e.g., Nisi et al. 2018). In the present study, since lightning flashes are used instead, we define a CI event when a certain number of CG flashes (2–30) appeared in a  $0.125^\circ \times 0.100^\circ$  grid box and no CI events were reported within a radius of 50 km around it in the previous 90 min. Sensitivity tests show that the results are robust, with similar temporal distributions over a range of different thresholds of CG flashes, radii and periods. The spatiotemporal mask and the  $N \leq 30$  filter were designed trying to avoid CI detection in case of secondary convection (storms triggered by previous convection) and storms already in their mature stage.

As a first step, a high-resolution spatial distribution of CG flashes over the entire Alpine region is developed, based on the high-quality lightning detection network data provided by the EUCLID consortium. The data cover the period 2005–19 and are aggregated in grid boxes of  $0.025^\circ \times 0.020^\circ$  every 10 min. Until now, detailed spatial and temporal distributions of lightning flashes were only provided for specific Alpine regions. An additional analysis (not shown) reveals that results do not qualitatively change if only the active times are analyzed (i.e., the 10-min periods when the lightning density is always 0 were excluded).

Consistent with Feudale and Manzato (2014), Punge et al. (2017) and Taszarek et al. (2020), a CG lightning hotspot is identified in northeastern Italy, suggesting the recurring presence of environmental conditions favorable to severe convection in the area. Other regions with intense lightning activity are identified in the Italian pre-Alps, in the Dinaric Alps, and in the northwestern coast of Italy (Liguria region). Conversely, a relative minimum of flash density coincides with the main Alpine crest. The maximum activity is observed between mid-May and mid-September, with a peak at the end of July. The diurnal cycle shows a maximum in the afternoon.

CI is studied on approximately  $10.1 \text{ km} \times 10.7 \text{ km}$  grid boxes (i.e.,  $5 \times 5$  aggregated CG grid boxes), an area large enough to represent a typical storm cell in its initial phase without dividing it over multiple grid boxes. The spatial distribution of CI partly overlaps (by definition) with that of CG lightning. However, peaks in CG lightning do not always equate to peaks in CI. The differences are likely associated with the presence of many thunderstorms originating in the Alpine/pre-Alpine areas, subsequently evolving into organized convective systems on the plain and coastal areas of the extreme northeast of Italy and western Slovenia (that are a reservoir of moist and warm air from the Adriatic Sea). Consequently, CIs are predominantly concentrated in the mountainous subareas of the domain, in particular in the part most exposed to low-level moist flows (i.e., southern slope of the Alps), while the peak in CG flashes occurs both in the mountains and downstream, i.e., on their eastern side (similar characteristics also emerge over the mountains of Bosnia and Herzegovina country), mainly associated with mature storms with higher lightning rates. The seasonal and diurnal cycles of CI are similar to those of the CG flashes, although the diurnal cycle peaks about one hour earlier and the interannual variability is

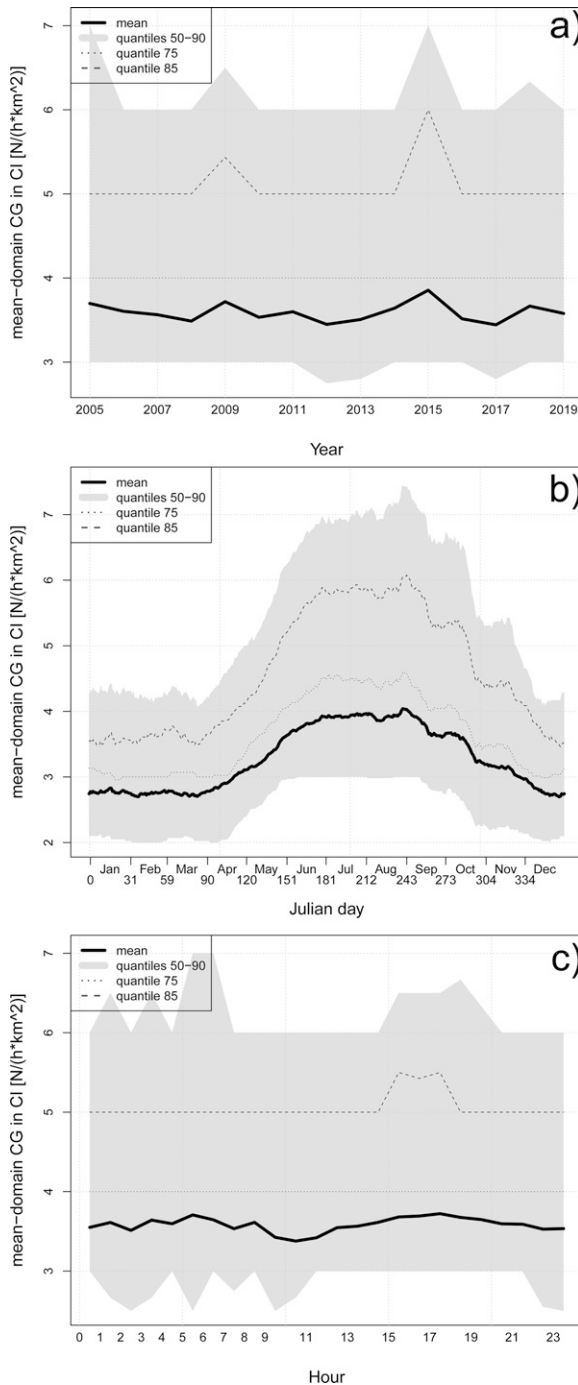


FIG. 15. Climatologies of the domain-averaged number of CG flashes from the subsample of the CI events studied in this work ( $\text{h}^{-1} \text{km}^{-2} \times 10^4$ ): (a) for each of the 15 studied years, for the year day together with a  $\pm 10$ -day moving average, and (c) for each hour of the day. The shaded area shows the interval between the 50th and 90th quantiles, while dotted and dashed lines show the 75th and 85th quantiles, respectively. Note that, despite the CG flashes per CI event are integer numbers, quantiles can be real numbers because they are computed interpolating the distribution.

much smaller. CI spatial distributions, obtained over 15 years using CG data only, were found to be very similar to those obtained over a shorter, 3-yr period, where CG and intra-cloud (IC) flash data were available (the [appendix](#)), suggesting that the use of CG alone does not clearly bias the results.

Considering the important role of the orography and the sea in modulating the spatial distribution, the climatology of CG and CI is also evaluated separately for three different subareas, which are classified considering both the terrain elevation and the distance from the sea: mountains, plains, and sea/coast. For each subarea, the frequency of CG and CI is calculated by year, day of year, and time of day. The temporal distribution of lightning flashes on the sea/coast is quite different from that inland. Overall, the lightning density on the sea/coast is small compared to the plains and mountains, and the difference is even greater in terms of CI. The peak of lightning activity and initiation in the mountains occurs mainly in late June and July. In autumn and winter, when the sea surface temperature becomes warmer than land (in particular during the night), the frequency of CG flashes and CI becomes higher on the sea/coastal areas.

The highest density of CG lightning is observed inland around 1500–1600 UTC (1 h earlier for CI). The diurnal cycle is much weaker on the sea/coast, and shows an opposite behavior, with a maximum in the night, possibly due to nocturnal land breeze, while it is most pronounced in mountainous areas, likely connected to thermally driven convergence of slope and valley breezes.

The comparison of the CI climatology with the CG-flash climatology facilitates the estimation of a bulk efficiency of CI in the production of CG flashes. Based on the standardized variables, fewer CG flashes per CI occur in May and between 1100 and 1200 UTC (1200–1300 local solar time). The efficiency is maximum between 1800 and 1900 UTC (1900–2000 solar), possibly due to storms that were initiated in the warmest hours and that were able to evolve in the following hours into larger and more organized systems. While the thermal orographic forcing for CI should be the strongest just after the peak of solar heating (1100 UTC), the potential instability is likely maximum few hours later and the combined effect of new storms and previous storms reaching their mature stage (concurring in a peak of CG flash production) is likely maximum in the late afternoon. Furthermore, a different efficiency occurs in the mountains, plains, and sea/coast subareas, possibly due to differences between maritime and continental clouds, characterized by different aerosol loadings.

The data also show a weak decreasing trend in the number of CG flashes during the 15 studied years, which is not statistically significant. In fact, a linear fit between years and annual mean of CG flashes shows only a small correlation, with a very low statistical significance. However, due to the limited extent of the time series, no signs of climate change can be clearly identified. The annual CG count and its high variability can be affected by changing in network configurations, instrumentation, and algorithm modifications to discriminate between IC and CG flashes (e.g., [Murphy et al. 2021](#)).

This study is the first to present together the climatology of lightning occurrence and convection initiation over the full pan-Alpine region. Many of our findings are consistent with past studies covering specific Alpine subregions, or larger regions including the Alps, implying that our methods pick up realistic variations in storm initiation and occurrence. At the same time, the study represents a fundamental step for the identification of sites of interest for the “Multi-scale Transport and Exchange processes in the Atmosphere over Mountains—program and eXperiment” (TEAMx; <http://www.teamx-programme.org>), whose observational campaign will be held in 2024–25. Considering that the Working Group on Orographic Convection has a specific interest in the study of convective initiation above mountainous terrain, the current spatial distribution of CI in the Alps has made it possible to identify some areas of particular interest for the campaign, such as the pre-Alpine areas in northeastern Italy, and the Sarntaler Alpen, corresponding to the isolated peak shown in Figs. 2 and 8 on the border between Austria and Italy (near the Merano label).

**Acknowledgments.** Thanks to ALDIS for having provided the CG EUCLID data. We thank the reviewers for fruitful discussion. The contributions of coauthor Kirshbaum were supported by a grant from Canada’s Natural Sciences and Engineering Research Council (RGPIN 418372-17). Stefano Serafin’s contribution to this research was funded by the Austrian Science Fund (FWF), Grant P30808-N32; a CC BY or equivalent license is applied to the author accepted manuscript and the version of record arising from this submission, in accordance with the grant’s open access conditions.

## APPENDIX

### Comparing CI Spatial Distribution from CG Alone or From Total Lightning Data

The majority of lightning produced by thunderstorms is in the form of IC flashes (cf. chapter 2 in Rakov and Uman 2003). To better study storm initiation, these data may be valuable (e.g., Schultz et al. 2011). For example, MacGorman et al. (2011) found that approximately only 65% of the studied storms had a CG flash within the first 10 min from the first detected IC flash. Since EUCLID IC flashes are homogeneously observed in the studied domain only since 2017, here we will compare the CI spatial distribution based on the  $4.8 \times 10^6$  CG-only flashes with that of the  $14.2 \times 10^6$  IC + CG flashes observed during the same period, i.e., years 2017–19.

Figure A1a shows the 2017–19 CI spatial distribution based on CG flashes, from the same algorithm used in Fig. 8 for the 2005–19 period. Comparing the two figures, the distribution in Fig. A1a is much more scattered, because of the very short period involved. If one computes CI using the total flashes (Fig. A1b) then the pattern is very similar to that of Fig. A1a, even if the total number of CI events detected is about 23% larger. However, one should consider that the filter on  $N$ , used to define a CI event, was based on the distribution of CG only flashes (Fig. 7). Considering the distribution of total

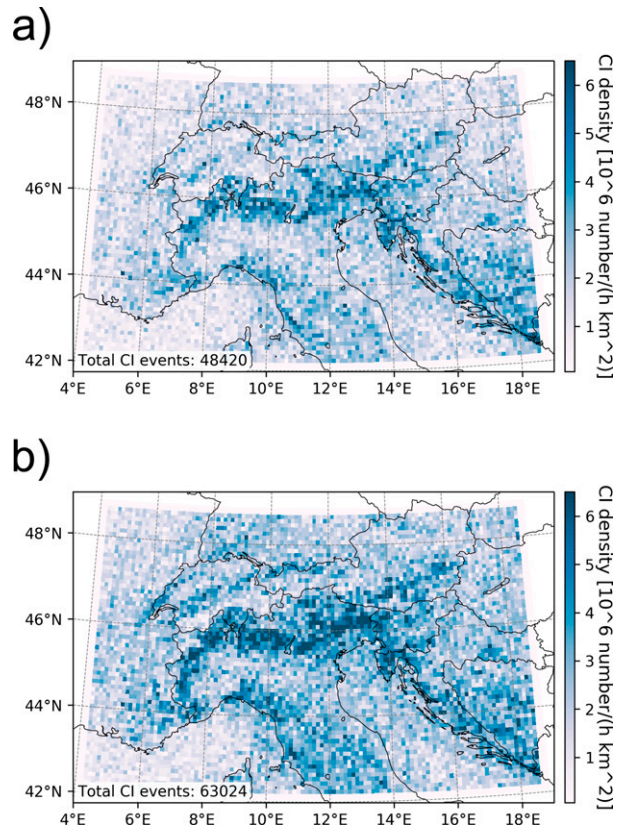


FIG. A1. The CI spatial distribution during years 2017–19 using (a) EUCLID CG flashes alone or (b) using EUCLID total (CG + IC) flashes. In both cases  $R = 50$  km,  $D = 90$  min, and  $2 \leq N \leq 30$ .

flashes, which are about 3 times more frequent than CG alone even in the first 10 min of storm life, one could choose larger thresholds on  $N$  and hence decrease the total number of CI events.

## REFERENCES

- American Meteorological Society, 2021: Thunderstorm. Glossary of Meteorology, <http://glossary.ametsoc.org/wiki/Thunderstorm>.
- Anderson, G., and D. Klugmann, 2014: A European lightning density analysis using 5 years of ATDnet data. *Nat. Hazards Earth Syst. Sci.*, **14**, 815–829, <https://doi.org/10.5194/nhess-14-815-2014>.
- Banta, R. M., and C. B. Schaaf, 1987: Thunderstorm genesis zones in the Colorado Rocky Mountains as determined by traceback of geosynchronous satellite images. *Mon. Wea. Rev.*, **115**, 463–476, [https://doi.org/10.1175/1520-0493\(1987\)115<0463:TGZITC>2.0.CO;2](https://doi.org/10.1175/1520-0493(1987)115<0463:TGZITC>2.0.CO;2).
- Bertram, I., and G. J. Mayr, 2004: Lightning in the eastern Alps 1993–1999. Part I: Thunderstorm tracks. *Nat. Hazards Earth Syst. Sci.*, **4**, 501–511, <https://doi.org/10.5194/nhess-4-501-2004>.
- Biagi, C. J., K. L. Cummins, K. E. Kehoe, and E. P. Krider, 2007: National Lightning Detection Network (NLDN) performance in southern Arizona, Texas, and Oklahoma in 2003–2004. *J. Geophys. Res.*, **112**, D05208, <https://doi.org/10.1029/2006JD007341>.

- Christian, H. J., and Coauthors, 2003: Global frequency and distribution of lightning as observed from space by the Optical Transient Detector. *J. Geophys. Res.*, **108**, D14005, <https://doi.org/10.1029/2002JD002347>.
- Costa, S., P. Mezzasalma, V. Levizzani, P. P. Alberoni, and S. Nanni, 2001: Deep convection over northern Italy: Synoptic and thermodynamic analysis. *Atmos. Res.*, **56**, 73–88, [https://doi.org/10.1016/S0169-8095\(00\)00091-0](https://doi.org/10.1016/S0169-8095(00)00091-0).
- Cummins, K., and M. J. Murphy, 2009: An overview of lightning locating systems: History, techniques, and data uses, with an in-depth look at the US NLDN. *IEEE Trans. Electromagn. Comput.*, **51**, 499–518, <https://doi.org/10.1109/TEMC.2009.2023450>.
- Deierling, W., and W. A. Petersen, 2008: Total lightning activity as an indicator of updraft characteristics. *J. Geophys. Res.*, **113**, D16210, <https://doi.org/10.1029/2007JD009598>.
- Diendorfer, G., H. Pichler, and W. Schulz, 2014: EUCLID located strokes to the Gaisberg tower—Accuracy of location and its assigned confidence ellipse. *23rd Int. Lightning Detection Conf. and Fifth Int. Lightning Meteorology Conf. (ILDC/ILMC)*, Tucson, AZ, Vaisala, 5 pp., <https://www.vaisala.com/sites/default/files/documents/Diendorfer%20et%20al-EUCLID%20Located%20Strokes%20to%20the%20Gaisberg%20Tower-2014-ILDC-ILMC.pdf>.
- Dixon, M., and G. Wiener, 1993: TITAN: Thunderstorm Identification, Tracking, Analysis, and Nowcasting—A radar-based methodology. *J. Atmos. Oceanic Technol.*, **10**, 785–797, [https://doi.org/10.1175/1520-0426\(1993\)010<0785:TTITAA>2.0.CO;2](https://doi.org/10.1175/1520-0426(1993)010<0785:TTITAA>2.0.CO;2).
- Enno, S.-E., J. Sugier, R. Alber, and S. Mark, 2020: Lightning flash density in Europe based on 10 years of ATDnet data. *Atmos. Res.*, **235**, 104769, <https://doi.org/10.1016/j.atmosres.2019.104769>.
- Feudale, L., and A. Manzato, 2014: Cloud-to-ground lightning distribution and its relationship with orography and anthropogenic emissions in the Po Valley. *J. Appl. Meteor. Climatol.*, **53**, 2651–2670, <https://doi.org/10.1175/JAMC-D-14-0037.1>.
- , —, and S. Micheletti, 2013: A cloud-to-ground lightning climatology for north eastern Italy. *Adv. Sci. Res.*, **10**, 77–84, <https://doi.org/10.5194/asr-10-77-2013>.
- Finke, U., and T. Hauf, 1996: The characteristics of lightning occurrence in southern Germany. *Beitr. Phys. Atmos.*, **69**, 361–374.
- Galanaki, E., K. Lagouvardos, V. Kotroni, E. Flaounas, and A. Argiriou, 2018: Thunderstorm climatology in the Mediterranean using cloud-to-ground lightning observations. *Atmos. Res.*, **207**, 136–144, <https://doi.org/10.1016/j.atmosres.2018.03.004>.
- Hagen, M., H.-H. Schiesser, and M. Dorninger, 2000: Monitoring of mesoscale precipitation systems in the Alps and the Northern Alpine foreland by radar and rain gauges. *Meteor. Atmos. Phys.*, **72**, 87–100, <https://doi.org/10.1007/s007030050008>.
- Hirt, M., G. C. Craig, S. A. K. Schäfer, J. Savre, and R. Heinze, 2020: Cold-pool-driven convective initiation: Using causal graph analysis to determine what convection-permitting models are missing. *Quart. J. Roy. Meteor. Soc.*, **146**, 2205–2227, <https://doi.org/10.1002/qj.3788>.
- Kaltenböck, R., and M. Steinheimer, 2015: Radar-based severe storm climatology for Austrian complex orography related to vertical wind shear and atmospheric instability. *Atmos. Res.*, **158–159**, 216–230, <https://doi.org/10.1016/j.atmosres.2014.08.006>.
- Kaňák, J., L. Okon, L. Méri, and M. Jurašek, 2020: Fully automated quantitative estimation of cloud top height using stereoscopic Meteosat dual satellite observations. *Space Research in Slovakia 2018–2019*, I. Dorotovič and J. Feranec, Eds., National Committee of COSPAR in Slovak Republic, Slovak Academy of Sciences, 70–81.
- Kingfield, D. M., K. M. Calhoun, and K. M. de Beurs, 2017: Antenna structures and cloud-to-ground lightning location: 1995–2015. *Geophys. Res. Lett.*, **44**, 5203–5212, <https://doi.org/10.1002/2017GL073449>.
- Kirshbaum, D. J., B. Adler, N. Kalthoff, C. Barthlott, and S. Serafin, 2018: Moist orographic convection: Physical mechanisms and links to surface-exchange processes. *Atmosphere*, **9**, 80, <https://doi.org/10.3390/atmos9030080>.
- Kober, K., and A. Tafferner, 2009: Tracking and nowcasting of convective cells using remote sensing data from radar and satellite. *Meteor. Z.*, **18**, 75–84, <https://doi.org/10.1127/0941-2948/2009/359>.
- Kotroni, V., and K. Lagouvardos, 2016: Lightning in the Mediterranean and its relation with sea-surface temperature. *Environ. Res. Lett.*, **11**, 034006, <https://doi.org/10.1088/1748-9326/11/3/034006>.
- MacGorman, D. R., I. R. Apostolopoulos, N. R. Lund, N. W. S. Demetriades, M. J. Murphy, and P. R. Krehbiel, 2011: The timing of cloud-to-ground lightning relative to total lightning activity. *Mon. Wea. Rev.*, **139**, 3871–3886, <https://doi.org/10.1175/MWR-D-11-00047.1>.
- Manzato, A., 2007: The 6 hours climatology of thunderstorms and rainfalls in the Friuli Venezia Giulia Plain. *Atmos. Res.*, **83**, 336–348, <https://doi.org/10.1016/j.atmosres.2005.08.013>.
- Markowski, P., and Y. Richardson, 2010: *Mesoscale Meteorology in Midlatitudes*. Wiley, 430 pp.
- Mecikalski, J. R., and K. M. Bedka, 2006: Forecasting convective initiation by monitoring the evolution of moving cumulus in daytime GOES imagery. *Mon. Wea. Rev.*, **134**, 49–78, <https://doi.org/10.1175/MWR3062.1>.
- Meyer, V. K., H. Höller, and H. D. Betz, 2013: Automated thunderstorm tracking: Utilization of three-dimensional lightning and radar data. *Atmos. Chem. Phys.*, **13**, 5137–5150, <https://doi.org/10.5194/acp-13-5137-2013>.
- Miglietta, M. M., A. Manzato, and R. Rotunno, 2016: Characteristics and predictability of a supercell during HyMeX SOP1. *Quart. J. Roy. Meteor. Soc.*, **142**, 2839–2853, <https://doi.org/10.1002/qj.2872>.
- Mohr, S., J. Wandel, S. Lenggenhager, and O. Martius, 2019: Relationship between atmospheric blocking and warm-season thunderstorms over western and central Europe. *Quart. J. Roy. Meteor. Soc.*, **145**, 3040–3056, <https://doi.org/10.1002/qj.3603>.
- Murphy, M. J., J. A. Cramer, and R. K. Said, 2021: Recent history of upgrades to the U.S. National Lightning Detection Network. *J. Atmos. Oceanic Technol.*, **38**, 573–585, <https://doi.org/10.1175/JTECH-D-19-0215.1>.
- Nisi, L., O. Martius, A. Hering, M. Kunz, and U. Germann, 2016: Spatial and temporal distribution of hailstorms in the Alpine region: A long-term, high resolution, radar-based analysis. *Quart. J. Roy. Meteor. Soc.*, **142**, 1590–1604, <https://doi.org/10.1002/qj.2771>.
- , A. Hering, U. Germann, and O. Martius, 2018: A 15-year hail streak climatology for the Alpine region. *Quart. J. Roy. Meteor. Soc.*, **144**, 1429–1449, <https://doi.org/10.1002/qj.3286>.
- , —, K. Schroeder, H. Barras, M. Kunz, and O. Martius, 2020: Hailstorms in the Alpine region: Diurnal cycle, 4D-characteristics, and the nowcasting potential of lightning properties. *Quart. J. Roy. Meteor. Soc.*, **146**, 4170–4194, <https://doi.org/10.1002/qj.3897>.
- Orville, R. E., and R. W. Henderson, 1986: Global distribution of midnight lightning: December 1977 to August 1978. *Mon. Wea. Rev.*, **114**, 2640–2653, [https://doi.org/10.1175/1520-0493\(1986\)114<2640:GDOMLS>2.0.CO;2](https://doi.org/10.1175/1520-0493(1986)114<2640:GDOMLS>2.0.CO;2).

- Pédeboy, S., E. Defer, and W. Schulz, 2014: Performance of the EUCLID network in cloud lightning detection in the South-East France. *Eighth HyMeX Workshop*, Valletta, Malta, CNRS and Météo-France.
- Piper, D., and M. Kunz, 2017: Spatiotemporal variability of lightning activity in Europe and the relation to the North Atlantic Oscillation teleconnection pattern. *Nat. Hazards Earth Syst. Sci.*, **17**, 1319–1336, <https://doi.org/10.5194/nhess-17-1319-2017>.
- Poelman, D. R., W. Schulz, and C. Vergeiner, 2013: Performance characteristics of distinct lightning detection networks covering Belgium. *J. Atmos. Oceanic Technol.*, **30**, 942–951, <https://doi.org/10.1175/JTECH-D-12-00162.1>.
- , —, G. Diendorfer, and M. Bernardi, 2016: The European lightning location system EUCLID—Part 2: Observations. *Nat. Hazards Earth Syst. Sci.*, **16**, 607–616, <https://doi.org/10.5194/nhess-16-607-2016>.
- Pucillo, A., M. M. Miglietta, K. Lombardo, and A. Manzato, 2020: Application of a simple analytical model to severe winds produced by a bow echo-like storm in northeast Italy. *Meteor. Appl.*, **27**, e1868, <https://doi.org/10.1002/met.1868>.
- Punge, H. J., K. M. Bedka, M. Kunz, and A. Reinbold, 2017: Hail frequency estimation across Europe based on a combination of overshooting top detections and the ERA-Interim reanalysis. *Atmos. Res.*, **198**, 34–43, <https://doi.org/10.1016/j.atmosres.2017.07.025>.
- Rakov, V., and M. Uman, 2003: *Lightning: Physics and Effects*. Cambridge University Press, 687 pp.
- Ren, T., A. D. Rapp, S. L. Nasiri, J. R. Mecikalski, and J. Apke, 2018: Is the awareness of the aerosol state useful in predicting enhanced lightning for lightning-producing storms over northern Alabama? *J. Appl. Meteor. Climatol.*, **57**, 1663–1681, <https://doi.org/10.1175/JAMC-D-17-0182.1>.
- Reynolds, S., M. Brook, and M. F. Gourley, 1957: Thunderstorm charge separation. *J. Meteor.*, **14**, 426–436, [https://doi.org/10.1175/1520-0469\(1957\)014<0426:TCS>2.0.CO;2](https://doi.org/10.1175/1520-0469(1957)014<0426:TCS>2.0.CO;2).
- Rosenfeld, D., 1987: Objective method for analysis and tracking of convective cells as seen by radar. *J. Atmos. Oceanic Technol.*, **4**, 422–434, [https://doi.org/10.1175/1520-0426\(1987\)004<0422:OMFAAT>2.0.CO;2](https://doi.org/10.1175/1520-0426(1987)004<0422:OMFAAT>2.0.CO;2).
- Saunders, C. P. R., H. Bax–Norman, C. Emersic, E. E. Avila, and N. E. Castellano, 2006: Laboratory studies of the effect of cloud conditions on graupel/crystal charge transfer in thunderstorm electrification. *Quart. J. Roy. Meteor. Soc.*, **132**, 2653–2673, <https://doi.org/10.1256/qj.05.218>.
- Schultz, C. J., W. A. Petersen, and L. D. Carey, 2011: Lightning and severe weather: A comparison between total and cloud-to-ground lightning trends. *Wea. Forecasting*, **26**, 744–755, <https://doi.org/10.1175/WAF-D-10-05026.1>.
- Schulz, W., C. Vergeiner, H. Pichler, G. Diendorfer, and K. L. Cummins, 2012: Location accuracy evaluation of the Austrian lightning location systems ALDIS. *22nd Int. Lightning Detection Conf. and Fourth Int. Lightning Meteorology Conf. (ILDC/ILMC)*, Broomfield, CO, 5 pp., Vaisala, [https://www.aldis.at/fileadmin/user\\_upload/aldis/publication/2012/3\\_ILDC2012\\_Schulz.pdf](https://www.aldis.at/fileadmin/user_upload/aldis/publication/2012/3_ILDC2012_Schulz.pdf).
- , G. Diendorfer, S. Pedeboy, and D. R. Poelman, 2016: The European lightning location system EUCLID—Part I: Performance analysis and validation. *Nat. Hazards Earth Syst. Sci.*, **16**, 595–605, <https://doi.org/10.5194/nhess-16-595-2016>.
- Schwalt, L., S. Pack, and W. Schulz, 2020: Ground truth data of atmospheric discharges in correlation with LLS detections. *Electr. Power Syst. Res.*, **180**, 106065, <https://doi.org/10.1016/j.epr.2019.106065>.
- Senf, F., and H. Deneke, 2017: Satellite-based characterization of convective growth and glaciation and its relationship to precipitation formation over central Europe. *J. Appl. Meteor. Climatol.*, **56**, 1827–1845, <https://doi.org/10.1175/JAMC-D-16-0293.1>.
- Simon, T., N. Umlauf, A. Zeileis, G. J. Mayr, W. Schulz, and G. Diendorfer, 2017: Spatio-temporal modelling of lightning climatologies for complex terrain. *Nat. Hazards Earth Syst. Sci.*, **17**, 305–314, <https://doi.org/10.5194/nhess-17-305-2017>.
- Smith, R. B., P. Schafer, D. J. Kirshbaum, and E. Regina, 2009: Orographic precipitation in the tropics: Experiments in Dominica. *J. Atmos. Sci.*, **66**, 1698–1716, <https://doi.org/10.1175/2008JAS2920.1>.
- Soderholm, B., B. Ronalds, and D. J. Kirshbaum, 2014: The evolution of convective storms initiated by an isolated mountain ridge. *Mon. Wea. Rev.*, **142**, 1430–1451, <https://doi.org/10.1175/MWR-D-13-00280.1>.
- Steinacker, R., M. Dorninger, F. Wölfemaier, and T. Krennert, 2000: Automatic tracking of convective cells and cell complexes from lightning and radar data. *Meteor. Atmos. Phys.*, **72**, 101–110, <https://doi.org/10.1007/s007030050009>.
- Takahashi, T., 1978: Riming electrification as a charge generation mechanism in thunderstorms. *J. Atmos. Sci.*, **35**, 1536–1548, [https://doi.org/10.1175/1520-0469\(1978\)035<1536:REAACG>2.0.CO;2](https://doi.org/10.1175/1520-0469(1978)035<1536:REAACG>2.0.CO;2).
- , 1984: Thunderstorm electrification—A numerical study. *J. Atmos. Sci.*, **41**, 2541–2558, [https://doi.org/10.1175/1520-0469\(1984\)041<2541:TENS>2.0.CO;2](https://doi.org/10.1175/1520-0469(1984)041<2541:TENS>2.0.CO;2).
- Taszarek, M., and Coauthors, 2019: A climatology of thunderstorms across Europe from a synthesis of multiple data sources. *J. Climate*, **32**, 1813–1837, <https://doi.org/10.1175/JCLI-D-18-0372.1>.
- , J. T. Allen, T. Púčik, K. A. Hoogewind, and H. E. Brooks, 2020: Severe convective storms across Europe and the United States. Part II: ERA5 environments associated with lightning, large hail, severe wind, and tornadoes. *J. Climate*, **33**, 10263–10286, <https://doi.org/10.1175/JCLI-D-20-0346.1>.
- van Delden, A., 2001: The synoptic setting of thunderstorms in western Europe. *Atmos. Res.*, **56**, 89–110, [https://doi.org/10.1016/S0169-8095\(00\)00092-2](https://doi.org/10.1016/S0169-8095(00)00092-2).
- Walker, J. R., W. M. MacKenzie Jr., J. R. Mecikalski, and C. P. Jewett, 2012: An enhanced geostationary satellite-based convective initiation algorithm for 0–2-h nowcasting with object tracking. *J. Appl. Meteor. Climatol.*, **51**, 1931–1949, <https://doi.org/10.1175/JAMC-D-11-0246.1>.
- Wapler, K., 2017: The life-cycle of hailstorms: Lightning, radar reflectivity and rotation characteristics. *Atmos. Res.*, **193**, 60–72, <https://doi.org/10.1016/j.atmosres.2017.04.009>.
- Weckwerth, T. M., J. W. Wilson, M. Hagen, T. J. Emerson, J. O. Pinto, D. L. Rife, and L. Grebe, 2011: Radar climatology of the COPS region. *Quart. J. Roy. Meteor. Soc.*, **137**, 31–41, <https://doi.org/10.1002/qj.747>.
- Zheng, D., Y. Zhang, Q. Meng, L. Chen, and J. Dan, 2016: Climatological comparison of small- and large-current cloud-to-ground lightning flashes over southern China. *J. Climate*, **29**, 2831–2848, <https://doi.org/10.1175/JCLI-D-15-0386.1>.
- Zinner, T., H. Mannstein, and A. Tafferner, 2008: Cb-TRAM: Tracking and monitoring severe convection from onset over rapid development to mature phase using multi-channel Meteosat-8 SEVIRI data. *Meteor. Atmos. Phys.*, **101**, 191–210, <https://doi.org/10.1007/s00703-008-0290-y>.